https://doi.org/10.5194/egusphere-2025-3454
Preprint. Discussion started: 6 August 2025

A magnetogenic framework integrating planetary magnetism and heat

Koen Vogel[1]

[1]KRV, The Hague, 2582 AP, The Netherlands

Correspondence to: koenrvogel@gmail.com

Abstract. Planetary magnetic fields are commonly thought to be generated by a planet-interior dynamo, wherein convection cells convert mechanical to magnetic energy via induced electric currents. Europa and Callisto's fields however are spawned by currents that are induced by the magnetic flux generated during their passage through Jupiter's field, and are therefore generated via a magnetic to electric to magnetic energy conversion. The Earth-incident solar wind deformation of the geomagnetic field induces similar currents in Earth's Outer Core. This article documents how solar wind induced currents regenerate the geomagnetic field and how waste heat from their magnetogenesis causes regional geothermal anomalies. This newly developed Solar Wind Induced Electric Dynamo (SWIED) framework explains the presence, magnitude, geometry and stability of the Earth's dipolar and non-dipolar fields, as well as its current polarity. It clarifies the origins of Earth's fluid Outer and solid Inner Core, and offers realistic mechanisms for geomagnetic excursions and reversals, secular non-dipole drift, and solar signals in the geomagnetic power spectrum. It accounts for the areas of high surface heat flow that originate in the Outer Core, thereby establishing the link between magnetogenesis, volcanism and continental drift.

The Gas and Ice Giants' magnetic fields are very likely generated by similar SWIEDs, whose by-product is substantial magnetogenic waste heat that significantly contributes to emitted planetary radiation, largely explaining why these planets emit more energy than they receive through solar irradiation alone. The SWIED model rationalizes their magnetic field geometries and heat anomalies, and accurately hindcasts their magnetic field strengths from best-estimate input data.

1 Introduction

Planetary magnetic fields are commonly thought to be generated by a kinematic dynamo, wherein highly conductive planet-internal convection cells convert their mechanical energy into the electric currents that are required to induce planetary magnetic fields (Stanley, 2014). This mechanical-to-electric conversion theory however cannot straightforwardly explain most planetary magnetic field geometries, for example Saturn's axisymmetric dipolar and Neptune's non-axial offset-dipolar magnetic fields can only be generated by self-sustaining kinematic dynamos under some very large and improbable assumptions (Cowling, 1955; Kivelson & Bagenal, 2014; Kaiser & Tilgner, 2014). Similarly, a classic dynamo is highly unlikely for the many planets and satellites, for example Saturn (Marley & Fortney, 2014), whose highly conductive layers – their ferromagnetic cores - are currently stable against convection. In addition, kinematic dynamo theory has very limited predictive value: kinematic dynamo models must treat a convecting fluid's velocity field as fixed input rather than a dynamic variable as the models cannot calculate any deformation of the flow caused by the magnetic field, and therefore cannot capture the time-dependent behavior of a fully nonlinear, chaotic dynamo. The industries that rely on up-to-date geomagnetic field information, such as aviation and shipping, therefore rely on the empirical World Magnetic Model (NOAA, 2025) rather than a kinetic dynamo model forecast. Most proposed dynamos must assume a wide range of highly speculative and planet-specific chemical, thermal and mechanical power sources, whose existence is often solely inferred by the presence of a magnetic field, and whose magnitude and existence are often refuted by observations (e.g. Gubbins et al., 2003, for Earth). A summary of the proposed sources (Stanley, 2014):

- No credible kinematic energy source: Jupiter, Uranus, Neptune
- Negative buoyancy due to material hypothetically solidifying at the outer core boundary: Saturn ("Helium rain"), Ganymede ("Iron snow")
- Positive buoyancy due to thermo-compositional outer core heating: Mercury, Earth

It is highly improbable that this wide array of proposed thermal, chemical and mechanical power sources generate similar order-of-magnitude strength fields. In contrast, observations from Europa and Callisto conclusively prove that an entirely different type of power source, namely the magnetic flux generated during the satellites' passage through Jupiter's magnetic field, is powering their fields (Khuruna et al., 1998; Kivelson et al., 2000; Zimmer et al., 2000). It is very unlikely that two completely different power sources fueling two completely different (dynamo & induction) planetary processes are both able to generate highly similar planetary magnetic fields. This article therefore proposes a novel planetary magnetogenesis theory that draws inspiration from the Galilean satellites' magnetic field origins. The theory better explains the existence, magnitude, geometry, polarity and stability of Earth's dipolar and non-dipolar fields. It clarifies the origins of Earth's fluid Outer (OC) and solid Inner (IC) Cores, and offers realistic, non-random evolutional pathways for geomagnetic excursions and reversals, dipole strengthening and weakening, secular non-dipole drift, and solar signatures in the geomagnetic power spectrum. It accounts for the areas of high surface heat flow, such as near plate margins, that originate in the OC, and thereby establishes the link between geomagnetogenesis, volcanism and continental drift. The theory also allows the accurate prediction of the magnetic field strength of Earth, as well as the Gas (Jupiter, Saturn) and Ice (Uranus, Neptune) Giants, from best-estimate input data. It similarly clarifies the otherwise-inexplicable magnetic field geometries and heat anomalies of such "problematic" planets as Saturn and Neptune.

2 The Galilean Satellites' induced magnetic fields

Three of the four Galilean satellites support magnetic fields (Io is the exception; Stanley, 2014). Spacecraft flybys of Europa and Callisto provide unequivocal evidence that their fields are induced by Jupiter's magnetic field: their directionally-shifting magnetic dipoles are consistently anti-parallel to the ambient Jovian field (Khuruna et al., 1998; Kivelson et al., 2000; Zimmer et al., 2000), as is predicted for an induced field (Parkinson, 1983), and their magnetic fields display the apparent rotation (synodic) periodicity of Jupiter (11.23 h for Europa and 10.18 h for Callisto; Zimmer et al., 2000). Their main magnetogenic power source is therefore demonstrably the magnetic flux generated during their orbit through Jupiter's inclined and rotating field, that is their magnetic fields are powered by the magnetic interaction between the changing strength and direction of the ambient Jovian field and the satellites' own fields. This magnetic flux induces the time-variant, satellite-interior electric currents (Lenz-Faraday Law) that induce their magnetic fields (Ampère's Law).

If a perfectly conductive and magnetically permeable shell covered the surface of these satellites, then their induced fields, B_I, would exactly cancel out Jupiter's magnetic field, B_J, at the two points on the shell where the two fields are exactly anti-parallel to one another, that is where B_J is normal to the shell, at the dipoles of the induced field (Parkinson, 1983). Zimmer et al. (2000) derive an equation that correlates the instantaneous induced field, B_A, produced by a spherical shell of arbitrary conductivity (that is less than infinite conductivity) at time t, to the induced field of a perfectly conducting sphere:

$$\mathrm{B}_A\,(\mathrm{t}) \;=\; \mathrm{A}\,\mathrm{B}_I\,(\mathrm{t} - \phi/\omega) \qquad \text{(Eqn. 1)}$$

whereby B is the magnetic field, A is an amplitude scaling factor (efficiency of magnetogenesis ≤ 100%), ω the frequency of the primary field (B_J) oscillation, and ϕ is a phase shift (the induced field must lag behind B_J). Note that an important yet obscure role is played by the satellites' skin depth, the travel distance through the satellites' interiors at which the amplitude of the primary or induced electromagnetic (EM) flux falls to 1/e of its original value. If an inductor lies within a satellite, then the EM flux will suffer energy losses ($A < 1$) while travelling through its interior. The flyby data however indicate that both Callisto and Europa can be accurately modelled as perfectly conducting spheres ($A \simeq 1$; $\phi \simeq 0$; Zimmer et al., 2000), indicating that EM energy losses due to the satellite-interior absorption are insignificant. Zimmer et al. (2000) infer plausible inductors through hypothesizing possible conductivity σ and magnetic permeability μ value combinations from Ohm's law, Zimmer et al.'s skin depth equation

$$s = \sqrt{\frac{\mu\sigma\omega}{2}} \qquad \text{(Eqn. 2)}$$

and the fundamental equation of EM induction (Parkinson, 1983):

$$\nabla^2 \boldsymbol{B} = \mu\sigma\frac{\partial B}{\partial t} \qquad \text{(Eqn. 3)}$$

Zimmer at al. (2000) demonstrate that a 4 km (Callisto) / 7.5 km (Europa) thick hypothetical salt water shell inductor (conductivity σ = 2.75 S/m) sitting just below surface fit the magnetic field observations well.

However, Zimmer et al. use Eqn. 2 under the assumption that σ and μ can be treated as static parameters, that is not a function of frequency, which is an inappropriate simplification when determining non-ferromagnetic materials' absorption of EM waves with frequencies below 1 kHz, as such properties vary greatly with frequency (Ott, 2009; Schelkunoff, 1943). The μσ term in Eqns. 2&3 decreases rapidly with declining frequency for non-ferromagnetic materials, such as (Mantle) silicates, but decreases much less rapidly for ferromagnetic materials as the latter's μ(ω) increases more than their σ(ω) decreases (Ott, 2009; Schelkunoff, 1943). Experimental data suggest that absorption by non-magnetic shields is relatively insignificant for frequencies below 1 kHz (Ott, 2009). The ~2.5 10^{-5} Hz EM flux (periods of 11.23 h for Europa and 10.18 h for Callisto; Zimmer et al., 2000) generated by the satellites' orbit through the Jovian field therefore very likely passes through their low magnetic permeability (~1.3 x 10^{-6} N.A^{-2}) ice crusts, hypothetical salt water shells and silicate mantles without significant losses, ruling out their possible role as possible inductors. The low frequency EM flux can only be absorbed by a planet-interior, much larger magnetic permeability (~1.0 x 10^{-3} N.A^{-2}; Ott, 2009) ferromagnetic layer, e.g. a ferromagnetic core, where it will induce an electric current. In addition, ferromagnetic core conductivities are on the order of 6 x 10^5 S/m (Merrill et al., 1998), so suffer significantly less induction Ohmic heat losses than a 2.75 S/m salt water inductor, and therefore behave more like the perfect conductor that the data suggests is generating the satellites' magnetic fields ($A \simeq 1$; $\phi \simeq 0$). Earth's salt water oceans similarly fail to generate planet-wide magnetic fields (Kuvshinov, 2008). Callisto and Europa's ferromagnetic cores are therefore far more likely inductors than hypothetical satellite-interior salt-water shells.

Ganymede's magnetic field shows many similarities with its neighbors' fields: its dipole moment is also antiparallel to the ambient Jovian field and induction signatures are also observed (Stanley, 2014; Collins & Johnson, 2014; Kivelson & Bagenal, 2014). A magnetic flux power source therefore demonstrably plays a key role in its magnetogenesis, although Stanley (2014) suggests that a self-sustained kinematic dynamo driven by negatively buoyant "iron snow" solidifying at the outer core boundary also contributes to its magnetogenesis. Ganymede's induction signatures however suggest that similar to Europa and Callisto its field is powered by the magnetic flux generated during its passage through Jupiter's magnetic field, thereby obviating the need for another (kinematic dynamo) magnetogenic process powered by hypothetical energy sources.

3 The Solar Wind – Magnetosphere energy interactions

The EM flux generated during the Galilean satellites' orbits through Jupiter's varying magnetic field induces electric eddy currents that in turn induce dipole fields that are consistently anti-parallel to the ambient Jovian field. Earth-incident solar wind generates similar EM flux that the Maxwell equations dictate must induce electric currents, hereafter referred to as Solar Wind Induced Currents (SWICs), which in turn must induce a magnetic field. The following sections detail the physical process.

3.1 Earth's orbitally-forced magnetogenic power source

The solar wind consists of a stream of charged particles (primarily protons and electrons) that is ejected from the Sun's corona at supersonic speeds, and that is accompanied by stream-embedded EM energy (Gosling, 2014; Weissman, 2014; Zerbo & Richardson, 2015). The estimated average Earth-incident solar wind power of 5 TW (Dessler, 1974; Herman & Goldberg, 1978) falls within the range of the estimated 3.6-10 TW (Merrill et al., 1998; Verhoogen, 1980; Gubbins et al., 2003) necessary to power the geomagnetic field, and is similar to the estimated 4 TW of heat lost by the Outer Core to the Mantle (Verhoogen, 1980). Earth-incident solar wind energy is a plausible geomagnetic and geothermal power source. A solar (wind) geomagnetogenic power source clarifies a number of observations that are otherwise difficult to explain:

- The orbital forcing signatures observed in paleogeomagnetic intensity data (Vogel, 2025, submitted)
- The temporal coincidence of geomagnetic dipole strength maxima with the Oort, Wolf, and Maunder solar activity minima (see below)
- The covariance of geomagnetic data with solar cycles: geomagnetic power spectral lines cluster around 21.4 years (sunspot cycle; Currie, 1973) and 27 days (solar rotation cycle; Banks, 1969)
- geomagnetic jerks occur with 10-year intervals (sunspot cycle; De Michelis et al., 2005)
- geomagnetic variability covaries with solar wind strength (Crooker et al., 1977; Stamper et al., 1999)

3.2 The solar wind generated EM flux

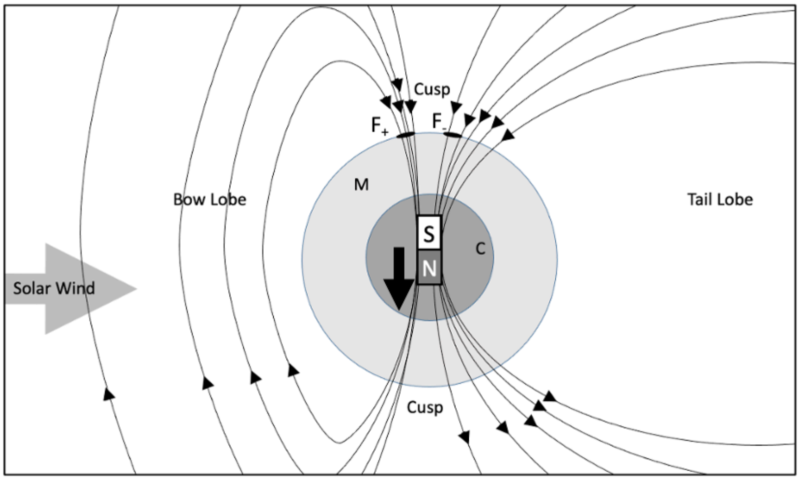

Figure 1: Schematic of how the Solar Wind deforms the geomagnetic field. C: Core; M: crust + mantle; Black ellipses in the Northern Hemisphere represent magnetic flux patches. F- and F+ are resp. negative and positive flux patches. The black arrow represents Earth's magnetic dipole moment. Not to scale.

https://doi.org/10.5194/egusphere-2025-3454
Preprint. Discussion started: 6 August 2025

For discussion purposes the following conventions are used: the Northern (NH) and Southern (SH) hemispheres lie resp. to the North and South of the (magnetic) equator; LT 12:00 (local time noon) is the meridian where the Sun is directly overhead, while LT 06:00, 00:00 and 18:00 refer to the meridians / positions resp. 90°, 180°, and 270° longitude to the west of the LT 12:00 meridian. Magnetic fields / moments are represented using oriented field lines / arrows (e.g. Fig. 1) that for a given location describe the direction of the magnetic force on a north monopole: Earth's field lines therefore currently flow out of the SH and into the NH (Fig. 1, 2), while Earth's "normal" dipole moment is represented by an arrow pointing from its (SH north pole) core to its magnetic south pole (Fig. 1). The number of field lines per unit area is the magnetic flux density (unit = T), while increases/decreases in the magnetic flux density signify resp. positive/negative magnetic flux (unit = Wb).

The solar wind continually deforms the Earth's magnetosphere, compressing its windward, dayside direction into a bow lobe, and extending its leeward, nightside into a tail lobe (Kivelson & Bagenal, 2014; Fig. 1), thereby transferring its kinetic and magnetic energy to our magnetosphere as EM flux. The most commonly-used method for calculating the magnitude of this energy transfer is to use the work-energy principle, that is to consider the solar wind as tiny masses that collide with and transfer their kinetic and magnetic energy to the magnetosphere (Dessler 1974; Herman & Goldberg, 1978; Baker et al., 1997). Such an approach is numerically correct, but masks the physical mechanisms underlying the energy exchange, and accordingly obscures how the solar wind energy is converted to EM flux. A better approach is to use Poynting's theorem (Purcell & Morin, 2013). The Poynting vector, S, defines the power density as:

$$S = \frac{E \times B}{\mu} \qquad \text{(Eqn. 4)}$$

whereby μ is the magnetic permeability of the medium, and E and B are the electric and magnetic field resp. Poynting's theorem is a reformulation of the conservation of energy: for a specified volume the rate of energy transfer, $\frac{\partial u}{\partial t}$, equals the rate at which fields do work on the charges in the volume, J.E, plus the energy flow leaving the volume (divergence of S):

$$-\frac{\partial u}{\partial t} = J.E + \nabla S \qquad \text{(Eqn.5)}$$

whereby J is the current density. The charged solar wind particles' (protons, electrons, alpha particles, etc) movement into the geomagnetic field results in a force acting on the particles that is perpendicular to the local electric and magnetic fields, and therefore in their deflection (Eqn. 4). Ambient geomagnetic field energy is hereby converted into deflected particle kinetic energy, while incident particle kinetic and magnetic energy are transferred to the magnetosphere as a change in local magnetic field density, that is EM flux (Eqn. 5; Fig. 2). Similar to the Galilean satellites, this EM flux passes through our non-magnetic Mantle with minimal loss, and is absorbed by the ferromagnetic OC where it induces eddy currents (SWICs).

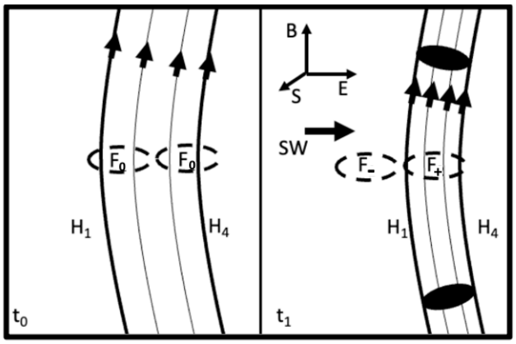

Figure 2: Schematic of how the solar wind compresses magnetic field lines on the bow side of a magnetosphere. SW: solar wind; H: magnetic field (H_1 and H_4 are field lines; B=μH); E: electric field. S: Poynting vector. F: space-stationary positive (+) and negative (-) flux patches. Left: time=t_0, before; Right: time=t_1, after solar wind impact

3.3 Geomagnetic deformation during the Solar Quiet

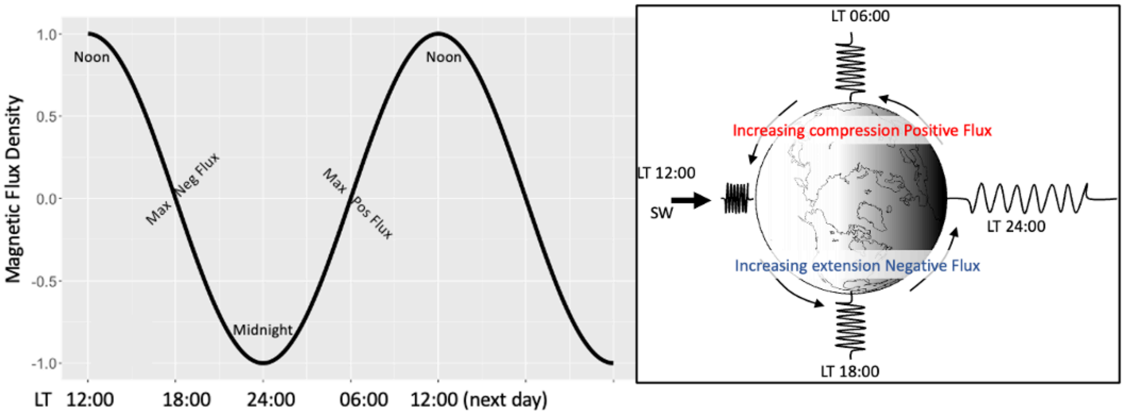

Figure 3: **left**: Idealized, normalized Earth surface magnetic flux density variation at high latitudes during the diurnal compression of the geomagnetic field by the solar wind; **right**: idealized compression and extension as viewed from space above the North Pole with the high latitude geomagnetic field deformation represented as a coiled spring.

At any given location on Earth the magnetic field can theoretically be expected to be experiencing compression between LT 24:00 (00:00; min compression) to LT 12:00 (max compression) (Fig. 3,4), and extension between LT 12:00 and 24:00. The idealized deformation process is conceptually similar to a rotating spring: the spring is fully compressed at LT 12:00, but restored to its undeformed state by LT 18:00, after which it is further extended until LT 24:00; fully extended at LT 00:00, but restored at LT 06:00, after which it is further compressed until LT 12:00. Due to Earth's rotation its magnetic field deformation continually shifts westward: the EM flux propagates as a four-dimensional (3D + time) wave, a flux oscillation with an extremely low frequency ω roughly equal to $(24\ \text{h} * 3600\ \text{s/h})^{-1} \approx 10^{-5}$ Hz (Fig. 3).

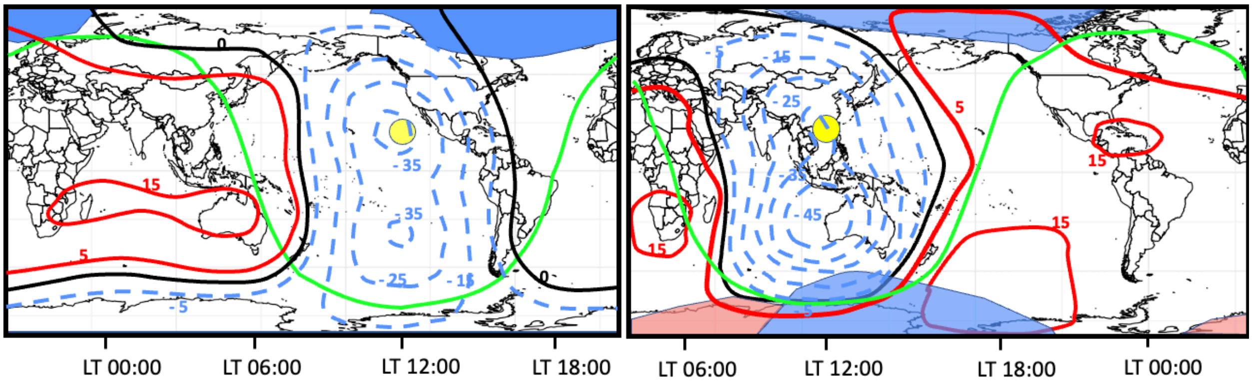

Figure 4: magnetic daily variation contours of the Solar Quiet total intensity (in nT) above the ionosphere at 20:30 UT (left) and 04:30 UT (right) derived from CHAMP satellite data (after Turner et al., 2007). Colored high latitude blobs represent observed high positive (red) and negative (blue) magnetic flux density changes. Yellow circle: solar direction; green line: daylight boundary. Note the undeformed field line (black line) near the ~LT 18:00 and ~LT06:00 meridians.

Magnetic flux is defined as the surface integral of the normal component of the magnetic field, so locations where the field lines penetrate the Earth's surface at a high angle, that is the high-latitude region "sweet spots" where inclination > 70° (Fig. 1, 4) experience greater EM flux variations than the equatorial regions (inclination ≈ 0°). The solar wind strength is time-variant, so the average of the 5 days of lowest monthly variations – the Solar Quiet - best represents the steady-state Earth-incident solar wind energy (Fig. 4). In Fig. 4 the areas of maximum magnetic compression (LT 12:00) occur just west of Mexico (left) and south of China (right), where the total geomagnetic intensity at the top of the ionosphere – somewhat counterintuitively - is lower: geomagnetic energy has been converted to solar wind kinetic deflection (Eqn. 4), lowering the local intensity value. The deformation contours are roughly symmetrical about the equator, as well as the LT 12:00 meridian, though the areas of high EM flux – at high latitude - are not. At UT 20:30 (Fig. 4 left) most of the solar wind generated EM flux is evidently being transferred as negative magnetic flux to an area to the northeast of North America, while the theoretically expected (Fig. 3) high-latitude areas of positive EM flux near LT 06:00 are absent. Fig. 4 (right) demonstrates that the SH shows a different behavior: at this date and time (04:30 UT) most of the NH solar wind generated EM flux is once again being transferred as negative EM flux, while in the SH a minor yet significant part is being transferred as positive EM flux between ~LT 12:00 and LT 00:00 (24:00).

3.4 SWIC circuit magnetogenic induction

The Lenz-Faraday and Ampère laws prescribe how the SWICs induce the geomagnetic field:

$$\nabla \times \mathrm{E} = F_E = -\frac{\partial B}{\partial t} \qquad \text{(Eqn. 6)}$$

$$\nabla \times \mathrm{H} = F_M = \frac{\partial D}{\partial t} + \mathrm{J} \qquad \text{(Eqn. 7)}$$

whereby F_E the electromotive force, F_M the magnetomotive force, D is the electric flux density, and H the magnetic field.

Eqns. 6 & 7 basically indicate that a time-variant magnetic field induces an electric field and vice versa. The negative sign in Eqn. 6 symbolizes a direction: a temporal change in a magnetic field induces a current (Eqn. 6) whose induced magnetic field (Eqn. 7) opposes (negative sign) the initial variation. A SWIC circuit therefore must generate a magnetic field (Fig. 5) that resists the magnetic deformation caused by the solar wind, that is one that counteracts the deformation and regenerates the undeformed geomagnetic field. In the case of a positive magnetic flux (Fig. 5 left) the magnetic flux density has increased and the SWIC must generate a field that opposes (destructively interacts with) this increase. The right hand rule determines the current in this SWIC circuit must therefore flow counter-clockwise, adding (conceptual) field lines (dotted circles) that in Fig. 5 come out of the page and destructively interact with positive flux. In the case of a negative magnetic flux (Fig. 5 right) the magnetic flux density has decreased (missing field lines), so the current in this SWIC circuit must flow clockwise in order to increase the magnetic flux density.

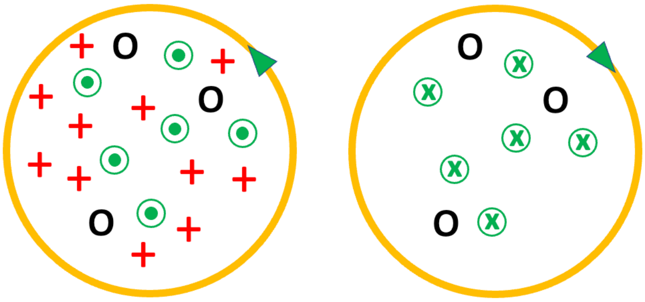

Figure 5: Schematic view of a SWIC circuit (orange circle) induced by positive (left) and negative (right) EM flux. All symbols within the circle except the dotted circles represent magnetic field lines flowing into the page. Black o's are "normal" geomagnetic field lines, red +'s are additional (positive magnetic flux) magnetic field lines. Green symbols are induced magnetic field lines: dotted / x'd circles represent induced field lines entering / leaving the page resp. Green arrow represents the direction of the induced current.

4 The Solar Wind Induced Electric Dynamo (SWIED) framework

A generic planetary magnetogenic framework, further referred to as the Solar Wind Induced Electric Dynamo (SWIED), takes its inspiration from the Galilean fields' magnetogenesis and the solar wind's deformation of the geomagnetic field. The solar wind deformation of a planet's magnetic field generates the EM flux that induces electric currents (SWICs) in its ferromagnetic core that induce the magnetic energy that (re)generates a planetary magnetic field. It differs from a kinematic dynamo in that the magnetogenic power source is the EM flux generated by the solar wind deformation of the magnetic field, not thermal or mechanical energy, and that the dynamo action is caused by the Earth's rotation, not randomly convecting currents. The path of the induced eddy currents take – their circuits – must conform to observations under either theory. The following sections detail Earth's induced current circuits, and details how these are better attributable to the solar wind generated EM flux and its resultant OC SWICs.

https://doi.org/10.5194/egusphere-2025-3454
Preprint. Discussion started: 6 August 2025

4.1 The SWIC induced geomagnetic field

If a perfectly conductive spherical shell covered the surface of an atmosphere-less Earth then its SWIC-induced field at solar equinox would be a dipole with an axis coincident with Earth's rotation axis (Parkinson, 1983). Variations of the induced dipole moment strength would then theoretically be a function of the solar wind strength, and variations in the induced dipole axis direction would be a function of the solar direction relative to Earth's rotation axis. In reality, the geomagnetic field does in fact largely resemble a dipole, whose moment varies with solar wind strength (see below), and whose axis is slightly inclined relative to the Earth's rotation (Gubbins & Love, 1998; Olson et al., 2006). So Earth's magnetogenic response to the SWICs broadly resembles the expected induced field. However, if Earth's OC did behave as a perfect conductor its geomagnetic dipole axis direction would show some seasonality, as the solar (wind) direction varies (relative to Earth's axis) during Earth's annual orbit when the overhead sun shifts between the Tropic of Cancer and the Tropic of Capricorn. The lack of observable seasonal dipole axis shifts therefore strongly suggests that the SWICs follow preferred current circuits that result in a quasi-steady-state geomagnetic dipole axis that can only slowly change through the gradual migration of the preferred SWIC circuits.

Earth's non-dipole field provides clues how Earth's OC behaves as an imperfect conductor. As time-variant EM flux cannot penetrate deep into the interior of a ferromagnetic conductor (Parkinson, 1983; Ott, 2009) these OC "imperfections" are likely located near the Core-Mantle Boundary (CMB). Some possible OC conductivity "imperfections" include:

- Chemical differences at the CMB, for example due to varying amounts of Sulphur or admixed mantle silicates
- CMB topography. The CMB depth fluctuates by up to 10 km around its hydrostatic equilibrium reference depth (Rodgers and Wahr, 1993; Morelli, 2007; Soldati et al., 2012).
- Temperature differences. Generally, the conductivity of ferromagnetic minerals such as iron decreases with increasing temperature due to increasing molecular vibrations (Isshiki and Igaki, 1978), though chemical variations (e.g. Sulphur and silicate content) and phase transitions (molecular state of iron) can complicate this picture.

OC energy sources power both the geomagnetic field as well as the estimated 4 TW of heat lost by the OC to the Mantle via the CMB (Verhoogen, 1980; Merrill et al., 1998). Magnetogenesis in nature can never be 100% efficient: for example, a kinematic dynamo's efficiency is likely on the order of 10-20% (Verhoogen, 1980; Merrill et al., 1998). Similarly, induction magnetogenesis suffers Ohmic heat losses in a non-perfect conductor. Therefore, a significant percentage of the energy of any magnetogenic process should be observable as its waste heat signature. Most surface-observed areas of high heat flow likely originate in the OC (Steinberger, 2000; Burke, 2011), so magnetogenic waste heat should be noticeable in most surface heat anomalies. An integrated approach towards better defining the preferred SWIC circuits consequently takes both geothermal and geomagnetic data - and their evident spatial and temporal covariation (Fig. 6) - into account.

https://doi.org/10.5194/egusphere-2025-3454
Preprint. Discussion started: 6 August 2025

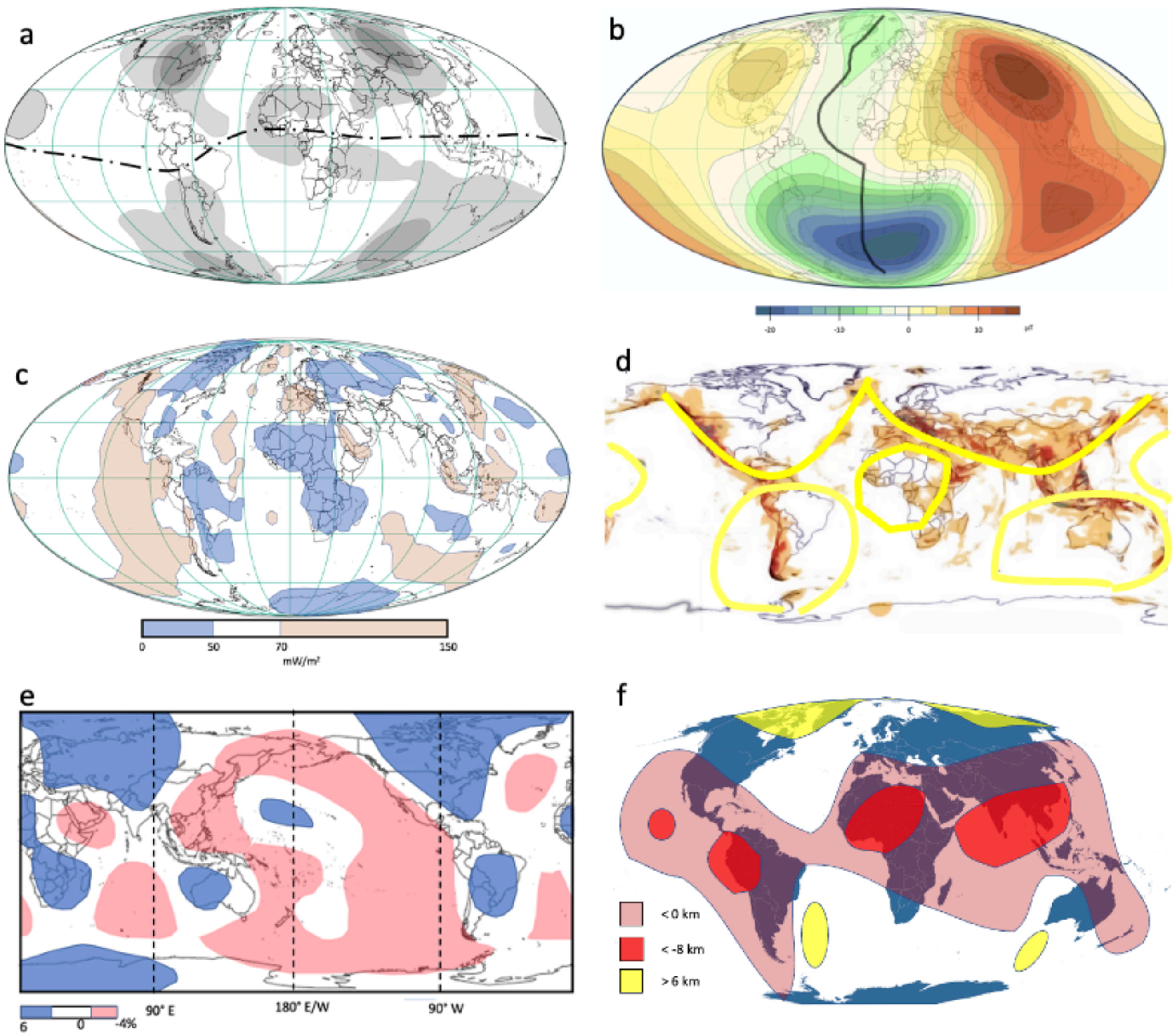

Figure 6: (a): 1690 to 1990 average of the radial component of the geomagnetic field squared (B_r^2) at the core surface (after Gubbins & Love, 1998); darker areas are higher; dot-dash line is magnetic equator. (b) Magnitude of the 1995 non-dipolar field (after Lühr, 2000); the black line represents the mid-Atlantic ridge. (c) the spherical harmonic expansion (to degree 36) of conductive heat flow (after Hamza et al., 2007). (d) Schematic of the preferred Solar Wind Induction Current circuits (yellow lines) on a World Geothermal Potential Map (after Coro and Trumpy, 2020; expert version); (e) 100 km deep seismic velocity anomalies from global mantle seismic tomography (after: Ekström & Dziewonski, 1998). Lower velocities (red) indicate higher mantle temperatures. (f) the spherical harmonic expansion (to degree 5) of a seismic model of long wavelength of CMB topography (after Rodgers and Wahr, 1993), derived from p-wave travel times. Colors represent differences in core radius with respect to hydrostatic equilibrium: red hues represent deeper depths.

Earth's SWICs almost certainly follow preferred current circuits - loops of least Ohmic resistance – along the CMB. These preferred SWIC circuits carry above-average SWIC intensities, J, and can therefore be expected to have:

- A strong induced radial magnetic field component, B_r, in the center of their CMB circuits, due to large J
- A large non-dipole anomaly at Earth's surface, over the center of their circuits, due to a large B_r
- Higher OC temperatures T_{CMB} along their CMB circuit peripheries, due to large J (Ohmic loss)
- CMB depth anomalies, due to variable T_{CMB}
- Lower overlying Mantle seismic velocities, due to higher T_{CMB}

4.2 Earth's preferred SWIC circuits

The best indicator of the locations of the preferred SWIC circuits is the historically average (1690-1990) geomagnetic radial field strength, B_r, as long-lived radial anomalies must lie centrally within the preferred current circuits along the CMB (Biot–Savart law). Fig. 6a shows 6 prominent circuit candidates: two NH mid-latitude (North America (NA), Eurasia(EA)), two SH mid-latitude (Oceania (O), South America (SA)), and two equatorial (mid-Pacific (MP), Africa(A)). The inferred SWIC circuit pattern (Fig. 6d) generates a geomagnetic octupole: a mid-latitude quadrupole (NH and SH SWIC circuits) that shares a center with a polar-equatorial quadrupole (the dipole's North (NM) and South (SM) magnetic poles with equatorial (MP, A) circuits). The relative stability of the geomagnetic field on annual to decadal timescales indicates that this octupole configuration interacts fairly consistently with the solar wind to produce a quasi-steady-state geomagnetic field through relatively long-lived preferred SWIC circuits. Note that in Fig. 6a the 4 mid-latitude quadrupole B_r patches all show protrusions towards the African circuit, as if the mid-latitude circuits are "sharing" radial energy with it: the combination of the moments of the mid-latitude quadrupole spawns the polar-equatorial quadrupole (see below).

Earth's non-dipole field (Fig. 6b) shows a large regional consistency with the inferred mid-latitude quadrupole (Fig. 6 a&d). The NH has two geomagnetic non-dipole (radial geomagnetic energy) highs centered around 55° N latitude and 90° W and 90° E longitude resp., locations that coincide with surface heat flow lows (Fig. 6 c-e). Both locations are in the center of their continental plates, remote from any hot, active plate margins, and form the bullseye of oblong radial field strength contours that are neatly bisected by the mid-Atlantic ridge geothermal anomaly that follows the geomagnetic non-dipole field strength saddle between the two highs, at ~90° longitude separation from each high.

An argument can be made that a relatively thick continental crust causes a lower surface heat flow than a thinner oceanic crust, but this cannot explain why – in a hemisphere that is ~60% covered by ocean – both geomagnetic non-dipole highs are located roughly at the center of continental plates. No plausible feedback mechanism exists between geomagnetogenesis and crustal composition or thickness, so the observed NH geomagnetic and geothermal geometries are likely caused by a single process – a magnetogenic SWIC circuit - that focuses radial magnetic energy at the center of continental plates while focusing waste heat at the plate margins, thereby – at least partially – also driving continental drift and volcanism (Verhoogen, 1980). Such reasoning could also explain why continental drift is absent on Earth's sister planet, Venus, whose magnetic field is weak to non-existent (Smrekar et al., 2014).

In the SH (~80% covered by ocean) the B_r highs (Fig. 6a) are also remote from hot plate boundaries, but their corresponding non-dipole centers (Fig. 6b) are more difficult to interpret due to the South Atlantic Anomaly (SAA), an area where the total field intensity is weakest relative to an idealized dipole field. The SAA roughly sits over the inferred SA SWIC circuit that therefore appears to cause a non-dipole minimum, not maximum. Both SH geothermal lows (Fig. 6c) and historical radial field strength highs (Fig. 6a) lie on roughly the same meridians as their NH quadrupole counterparts: they form the SH poles of the mid-latitude quadrupole. The 90° W and 90° E longitude lines also roughly coincide with the preferred virtual geographic pole (VGP) trajectories during recent magnetic reversals: transitional VGP paths are strongly biased to lie in the American 90° W meridian or its antipodal direction (McFadden & Merrill, 1995; Gubbins & Love, 1998; Merrill et al., 1998), suggesting that changes in mid-latitude SWIC circuit strengths play a key role during magnetic reversals.

The conductive heat flow and geothermal maps (Fig. 6 c-e) show large areas of low heat flow in the center of the preferred SWIC circuits, and high heat flow along their peripheries. The mid-Atlantic ridge for example meanders along the areas of high heating that form the SWIC circuit boundaries (Fig. 6d), strongly suggesting a causal link. Similarly, the low velocity anomalies from Ekström & Dziewonski's 1998 seismic tomography model (Fig. 6e; high Mantle heat flux correlates to low velocity) clearly outline the NH (NA, EA), SH (SA, O), and equatorial (A, MP) SWIC circuits. Note that Ekström and Dziewonski's 1998 study mainly focused on Mantle convection paths, not CMB heat anomalies, and that the seismic wave amplitude attenuation below 250 km depth causes deeper results to be progressively more uncertain. The same limitations apply to the CMB topography: Fig. 6f shows that the mid-latitude quadrupole centers largely correspond to CMB topographic highs (yellow areas), while the SWIC circuits largely follow topographic lows (red areas), possibly indicating higher CMB areas have lower conductivity e.g. due to a larger amount of silicate admixtures. While Fig. 6f was cherry-picked from the 3 largely dissimilar CMB topography reconstructions discussed by Morelli (2007), more recent reconstructions by Soldati et al., 2012 show similar patterns.

https://doi.org/10.5194/egusphere-2025-3454
Preprint. Discussion started: 6 August 2025

4.3 The mid-latitude geomagnetogenic quadrupole

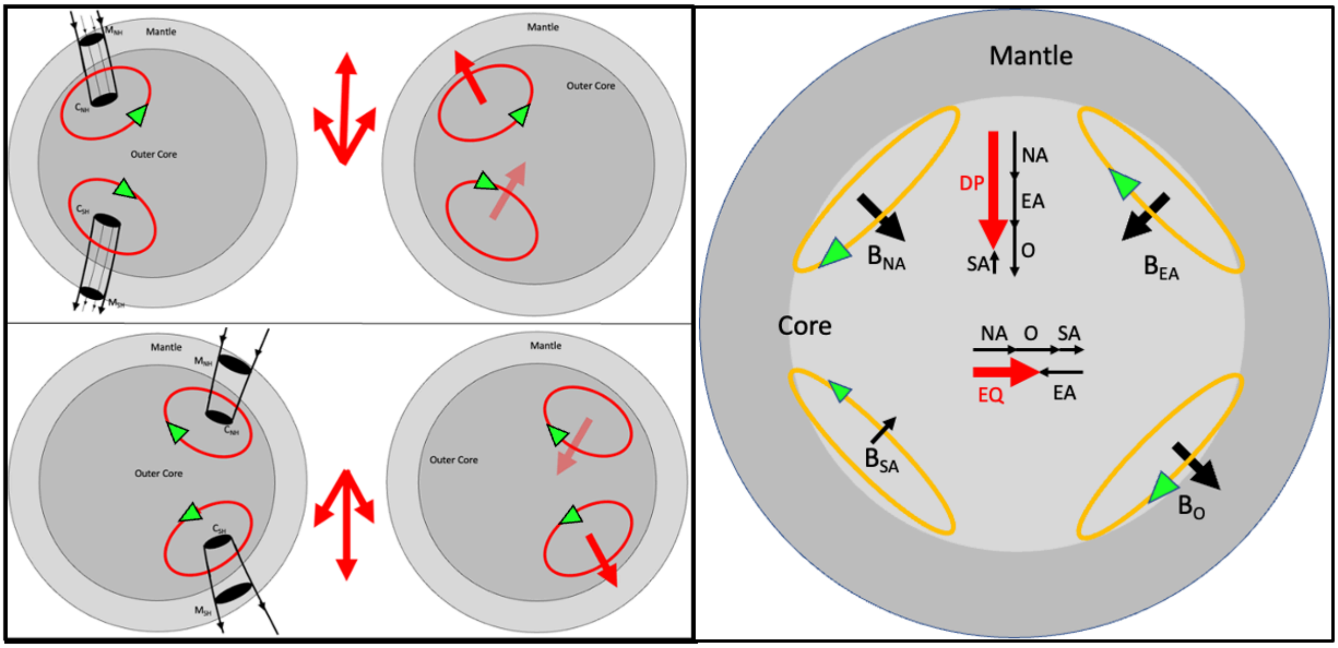

Figure 7: (left) schematic of how (top) positive magnetic flux generates a counterclockwise (as seen from the north) NH / SH SWIC circuit inductor pair, resulting in a “reverse” polarity field and (bottom) how negative magnetic flux generates clockwise SWIC circuit inductor pairs and a “normal” polarity field; Combined NH and SH SWIC circuit magnetic moments plotted next to the geographical equator. (right) schematic of how the mid-latitude quadrupole generates a mainly dipolar field, as well as the polar-equatorial quadrupole. Black lines: magnetic field lines; black ovals: flux patches. Red & orange loops: SWIC circuits. Thick red & black arrows: magnetic moments. Not to scale.

A classic quadrupole field consists of 4 equal strength poles (2 N & 2 S), whereby same polarity poles sit diametrically opposite each other. Earth’s mid-latitude quadrupole however is (re)generating a geomagnetic field that resembles a dipole. In the NH the EA SWIC circuit spans the 170º E – 20º W latitude range while the NA circuit spans the 20º W to 150º W range (Fig. 6d), leaving only a small 40º longitude window between the two. This window is almost certainly characterized by a minor high-latitude SWIC circuit, whose arcuate magnetogenic waste heat is responsible for the Kuril Island volcanic archipelago. The broad width of the EA and NA SWIC circuits causes the mainly negative (Fig. 4) NH solar wind generated EM flux to be mostly shared between the two circuits. For example in Fig. 8 (left) at 20:30 UT the NA circuit is receiving the bulk of the mainly negative magnetic flux, but the EA circuit is still receiving – and had been receiving since ~UT 00:00 – significant negative EM flux. At UT 20:30 the NA and EA SWIC clockwise circuits are inducing magnetic energy that partially regenerates the geomagnetic field, that is provides the magnetic counterpressure to the solar wind deformation.

https://doi.org/10.5194/egusphere-2025-3454
Preprint. Discussion started: 6 August 2025

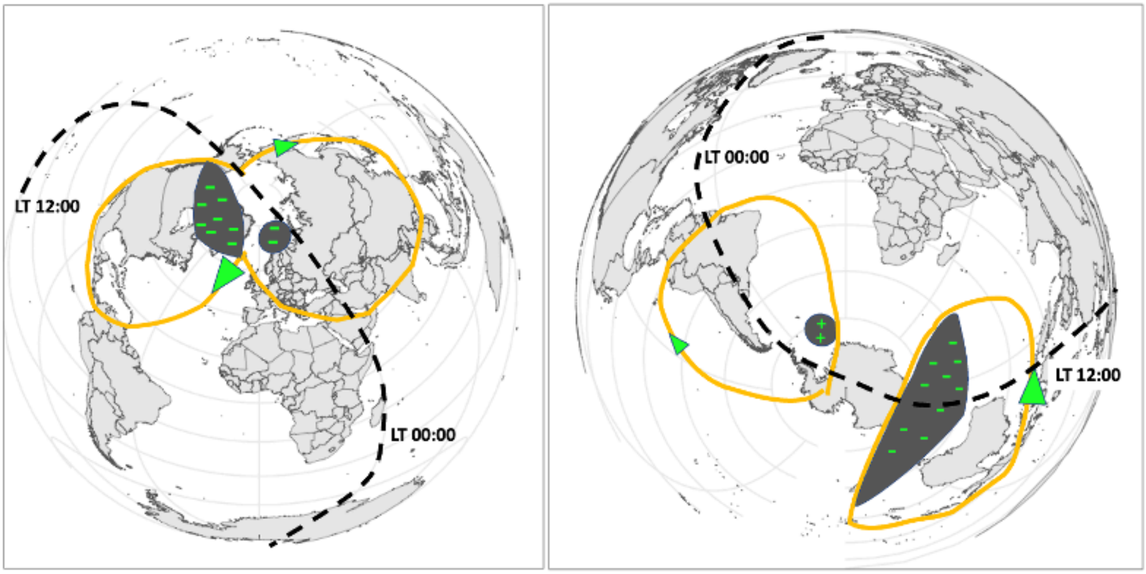

Figure 8: schematic of how the mid-latitude quadrupole SWIC loops (re)generate the geomagnetic field at 20:30 UT (NH; left) and 04:30 UT (SH; right) (ref: Fig. 4).

The lack of positive EM flux transfer and the longitudinal symmetry of the solar wind deformation in Fig. 4 (left) implies that while the LT 12:00 - ~LT 16:00 area is actively being deformed by the solar wind (negative flux energy transfer) the area between LT 12:00 - ~LT 08:00 is actively being restored to its normal magnetic intensity by the combined mid-latitude quadrupole induced field. As the magnetic field lines have a positive inclination in the NH (go into the page in Fig. 5 & 8 left), the NA / EA SWICs circuit in a clockwise direction (Iceland -> Alaska / Kamchatka -> Iceland), which induces magnetic field moments that flow into the Earth in the NH (Fig. 7 (left bottom)), thereby locally counterbalancing the decrease in magnetic flux density (Fig. 5 (right)), but also (re)generating the "normal polarity" geomagnetic field (Fig. 7 (right)). To the east of the LT 12:00 line the solar wind is deforming the geomagnetic field and transferring flux, to the west the NA and EA SWIC circuits are actively preventing deformation. The magnetic energy generated in a NH mid-latitude quadrupole circuits combines with their paired SH counterparts: as they lie on the same meridian, they simultaneously experience the solar wind generated EM flux, so the two act as paired inductors (Fig. 7 left).

If the solar wind also exclusively generated negative EM flux in the SH in the idealized case in Fig. 9 (right), then the midlatitude quadrupole would generate a "normal" polarity dipole field (Fig. 7) with 4 equal-strength non-dipole highs over the SWIC circuit centers and with a dipole axis that coincided with Earth's rotational axis. In reality however the SH mid-latitude SWIC circuits are not as longitudinally extensive as their NH counterparts: they extend from ~170º E - ~70º E (O) and from ~10 º W - ~90º W (SA). The large longitudinal windows in between the preferred SWIC circuits result in significant parts of the solar wind generated EM flux transferring as positive flux at UT 04:30 (Fig. 4 (right)). This positive flux causes an increase in magnetic flux density in the SA circuit and therefore a counterclockwise SA SWIC flow (Figs. 5

left, 8 right), resulting in a "reverse" polarity magnetic moment at UT 04:30. This positive magnetic EM flux is therefore directly responsible for the SAA: the "reverse" polarity SA magnetic moment destructively interferes with the "normal" magnetic moments of the other 3 quadrupoles (Fig. 7 right).

4.4 Magnetic field reversal

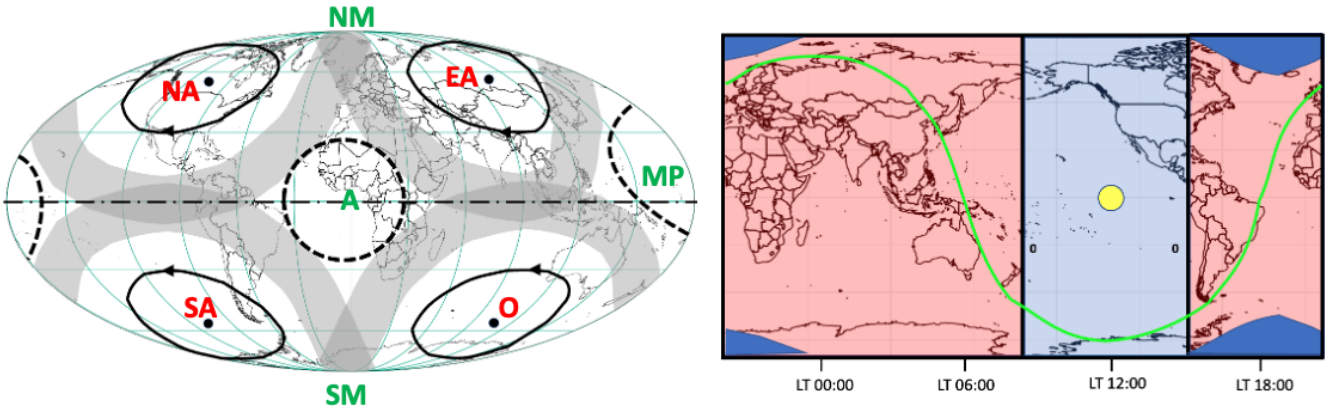

Figure 9: (left) schematic of an idealized geomagnetic octupole consisting of the mid-latitude quadrupole (red letters) and the polar-equatorial quadrupole (green letters); black arrows represent SWIC circuits, grey bands indicate areas of high heating; (right) idealized schematic of the Solar Quiet magnetic daily variation (ref: Fig. 4 left) above the ionosphere at 20:30 UT that generates a normal polarity magnetic field. Light blue is the area of solar wind compression (negative contours), light red is the area of the relatively undeformed geomagnetic field. Blue polar blobs represent high negative magnetic flux density changes; yellow circle: solar direction; green line: daylight boundary.

Figure 4 clearly illustrates that the Earth-incident solar wind energy is currently largely being transferred to the OC as negative EM flux, which results in predominantly clockwise circuiting SWIC currents, which in turn generate "normal" polarity magnetic moments that combine to form a "normal" dipole field, thereby regenerating the geomagnetic field and resisting positive EM flux transferal. This scenario however can easily be reversed: solar wind energy can equally well be entirely transferred as positive flux powering counterclockwise circuits that generate a "reverse" magnetic field. In such a case the area between LT ~08:00 - LT 12:00 in Fig. 9 (right) is progressively being compressed as the Earth rotates the LT ~08:00 position to LT 12:00, causing positive EM flux transfer, which in turn results in counterclockwise SWIC circuits that resist (generate magnetic counterpressure) the deformation of the LT 12:00 - ~ LT 16:00 area. There are numerous plausible pathways to reversal, but all involve considerable weakening to reversal of "normal" individual SWIC circuits, e.g. the NA circuit, leading to considerable weakening and reversal of an inductor pair, e.g. the NA/SA inductor pair, leading to a chaotic quadrupole period when EM flux is transferred in equal amounts as positive and negative flux, leading to a more stable period whereby the solar wind energy is predominately transferred as positive flux and the dipole is reversed.

https://doi.org/10.5194/egusphere-2025-3454
Preprint. Discussion started: 6 August 2025

Changes in the SWIC intensity cause variations in induced moment strengths, which in turn results in changes in the resultant quadrupole-generated dipole field intensity and axis direction (Fig. 7 right), which in turn influences how the solar wind transfers its EM flux. The relative strengthening and weakening of an individual SWIC circuit moment however has relatively little impact on their circuit trajectories or moment orientations. During a magnetic reversal their combined mid-latitude quadrupole magnetic moment vector, the resultant Virtual Geomagnetic Pole (VGP), will therefore always remain close to the 90° E & 90° W meridians that connect the SWIC circuit centers. Magnetic reversal VGP measurements therefore support the SWIED reversal model: transitional VGP paths are strongly biased to lie in the American 90° W meridian or its antipodal direction (McFadden & Merrill, 1995; Gubbins & Love, 1998; Merrill et al., 1998).

5 The properties of the Geomagnetic Field

5.1 The Outer Core Energy Budget

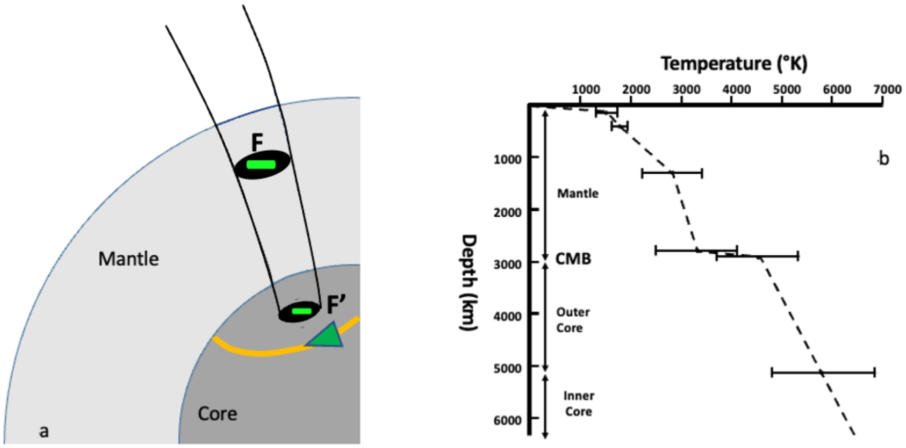

Figure 10: a) Idealized quarter-section through the Earth, showing a negative flux tube entering the OC (F') via the Mantle (F); orange arc & green arrow represent a clockwise, "normal" polarity SWIC circuit; b) geothermal gradient for 10a (dashed line) with the estimated temperature ranges (after Verhoogen, 1980)

The solar wind generates EM flux that is mostly absorbed by the OC, where it induces a current (SWIC) that in turn induces magnetic energy while losing Ohmic waste heat. This magnetic induction is almost certainly occurring in the outermost layer of the OC, as the EM flux cannot penetrate very far into a high-μσ ferromagnetic OC (Parkinson, 1983). Significant heating is also demonstrably occurring in the outer shell of the OC at the CMB, as some heating process must be maintaining the abnormally high 10-12 °C/km (Verhoogen, 1980) geothermal gradient immediately above it (Fig. 10b). The colocation of the heat and magnetic energy at the CMB strongly suggests they are both the result of the magnetogenic process. At the CMB this magnetogenic "waste" heat locally raises the OC temperature above its adiabatic Core melting curve, resulting in a fluid

https://doi.org/10.5194/egusphere-2025-3454
Preprint. Discussion started: 6 August 2025

OC and a lower-than-adiabatic temperature gradient through the Core, which at increased depth and pressure results in a solid (but soft) Inner Core (Verhoogen, 1980; Tkalčić & Phạm, 2018).

A flux-to-current-to-counterflux process can never be 100% efficient: in reality some energy will be lost as waste heat in the OC. Assuming that Mantle low-frequency flux losses are insignificant (see above) allows an estimation of the OC magnetogenic efficiency. Observations indicate that internal Earth-induced magnetic currents (reaction) at surface are roughly one third in size and opposite in direction (Matsushita & Maeda, 1965; Baker et al., 1997) to the daily geomagnetic variations (action), so as a first approximation the magnetogenic efficiency is ~0.33. If 2/3 of the solar wind generated EM flux is lost as Ohmic waste heat and if SWIC circuit resistivity increases with temperature, then geomagnetic field strength counterintuitively increases during periods of low solar wind strength. This has been confirmed by other studies (Aubert, 2020; Stacey and Davis., 2008; Verhoogen, 1980): the geomagnetic field strength increases when the OC cools. The heating and cooling of SWIC circuits, and the impact this has on their resistivities, therefore provides the main mechanism for the weakening and strengthening resp. of the individual SWIC circuit magnetic moments. Assuming an Earth-incident solar wind power of 5 TW (Dessler (1974)):

$$\text{OC heat losses} \; = \; 5\,TW - \frac{5TW}{3} \approx 3.4TW \qquad \text{(Eqn. 8)}$$

This approximation is highly similar to the estimated 4 TW of heat flux across the CMB (Verhoogen, 1980), especially if an updated solar wind power estimate of 6.4 TW (see below) is used.

5.2 The geo-SWIED: Earth's dipolar and non-dipolar fields

Figure 6b represents a 1995 "snap-shot" image of the continuously changing non-dipole field. When averaged over the 1690-1990 time period (Fig. 6a), the mid-latitude quadrupole becomes apparent due to the persistent radial field strength at the SWIC circuit centers over the past 300 years. The EA-O circuits, as well as the NA-SA circuits, are in paired inductance (Fig. 7), as the geomagnetic field lines that enter Earth's magnetosphere in the NH must exit in the SH (Gauss's law for magnetism), so these NH-SH paired inductors must jointly increase or decrease in strength.

The EA-O pair constructively interacts, as both circuits are powered by negative magnetic flux that induces clockwise SWICS (Fig.7 bottom, 8) and "normal" magnetic moments. The NA (clockwise; "normal") - SA (counterclockwise, "reverse") however destructively interact (Fig. 7, 8). Figure 11 indicates that over the last 120 years the NA-SA pair has been jointly decreasing in "normal" strength, while the EA-O pair has been jointly increasing. The paired inductance between the SWIC circuits is also evident in time-series animations of the total field strength between 1900-2020, for example, the NA and SA SWIC circuit total field strengths reduce in tandem. (https://geomag.colorado.edu/main-magnetic-field; their Fig. 3, accessed: 2025 June 19)

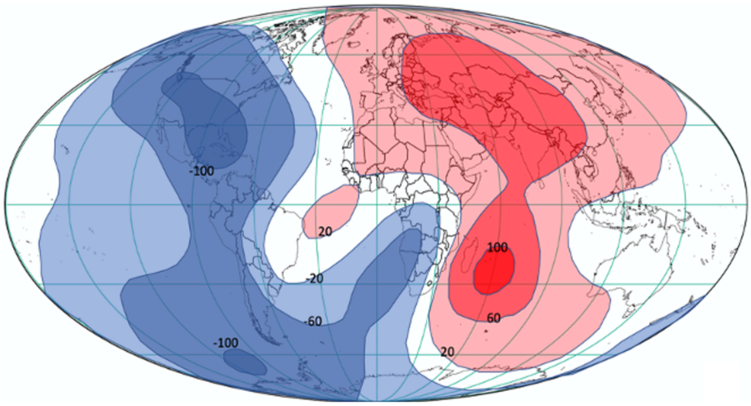

Figure 11: Annual rate of change of International Geomagnetic Reference Field Total Intensity between 1900-2020 (numbers are change in nT/year; After BGS, 2025a)

5.3 Global centennial variability

Figure 12: Historical Geomagnetic Dipole Moment ([dataset] GFZ, 2025) overlain by estimated solar minima periods (shaded columns; Source: Eddy 1976; Wu et al. 2018)

Three of the four major solar minima - Oort, Wolf, Spörer and Maunder – that have occurred during the last 1000 years (Eddy, 1976; Wu et al., 2018) are characterized – as expected – by geomagnetic dipole moment increases (Fig. 12), which allows another rough quantification of the amount of solar wind generated power that the Geo-SWIED allocates to heat generation and magnetic energy. During the Oort minimum the magnetic strength increased over 150 years, only to lose these gains over the next 100 years. Similarly, during the Maunder minimum the gains of 90 years were lost again over the next 50. Both increases and decreases occur in fairly linear fashion, and are therefore roughly consistent with an magnetogenic allocation of 1/3 to the magnetic energy and 2/3 to the "waste" heat, similar to what was found in Eqn. 8.

Solar maxima periods are characterized by OC heating, implying increasing amounts of OC heat must be shed to the overlying Mantle via the CMB during these periods. The solar minima periods show significant increases in volcanic activity (Fig. 13), which could therefore be plausibly caused by OC heat generated during the previous solar maxima that has made its way to surface. Assuming the OC heating reached a local maximum around ~1580 CE, midway between the end of the Spörer Minimum (~1550 CE) and the start of the decrease of OC temperature inferred from the geomagnetic dipole moment increase (~1610 CE; Fig. 12) would suggest OC-to-surface heat travel times of 30-60 years, as peak Maunder era large volcanic eruption density was reached around 1610-1640 (Fig. 13 left). This assumes a significant portion of the geothermal heat flux through the CMB occurs as (fast) radiative heat transmission, rather than (slow) lattice thermal conductive heat transfer, as has been demonstrated by Murakami et al. (2022) for radiative transfer at the CMB. Note that the relatively large post-Spörer dipole moment decrease of ~0.1 10^{22} Am^2 signifies a relatively large post-Spörer OC heating, possibly explaining the exceptionally large amount of volcanism during the Maunder minimum.

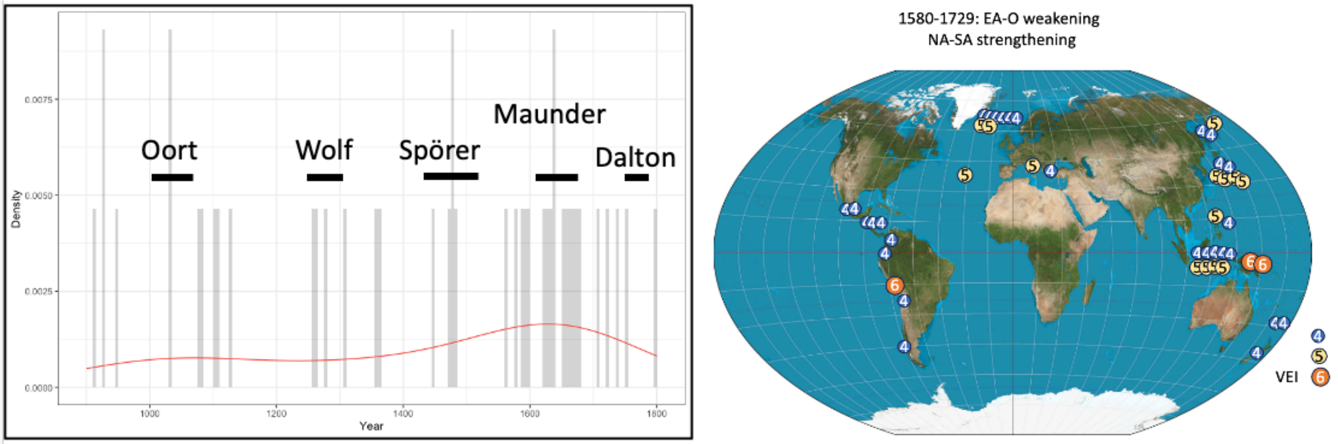

Figure 13: (left) Large (VEI ≥ 5) volcano eruptions (gray bars) and density (red line) over the CE 900-1800 period([dataset] Global Volcanism Program, 2024); black bars indicate solar minima periods; (right) locations of the Large (VEI ≥ 4)Volcanic eruptions between 1610-1729

The data suggest that since ~1750 an increase in solar activity has been causing geomagnetic and volcanic regimes shifts:

- The severity of solar minima decreased after the Maunder minimum (Eddy, 1976)
- The geomagnetic dipole moment has been monotonically decreasing since then ([dataset]* GFZ, 2025)
- The Large Volcano (VEI ≥ 5) frequency has remained steady (Smithsonian Institution, 2025)

5.4 Geo-SWIED: geomagnetic excursions

The geomagnetic field consists almost entirely of an inclined geocentric axial dipole (GAD) when averaged over super-millennial time periods (Merrill et al., 1998; Olson & Amit, 2006), although intervals of quasi-steady-state field geometries with constant polarity can be interrupted by magnetic reversals (rate: 2-3 per Ma), when the geomagnetic poles switch locations, as well as geomagnetic excursions (rate: 1 per 5-10 ka), when the magnetic pole directions significantly move away from the time-averaged dipole direction of the GAD (Gubbins, 1999; Olson & Amit, 2006). A spectrum of magnetic pole movements ranging from "large shift" (~5-10 per ka) to excursion (less common) to reversal (relatively uncommon) may exist, and the nomenclature becomes immaterial if the processes causing such variations are similar and also follow a spectrum: a large shift may then also be termed a minor excursion, a strong excursion may grade into a failed reversal, etc.

A weakening of the dipole moment accompanies many excursions and reversals (Gubbins, 1999; Olson & Amit, 2006) suggesting the weakening of a coupled SWIC inductor pair moment very likely causes these major magnetic pole movements. For example, the 1900-2020 weakening of the American SWIC induction pair (Fig. 11) resulted in the progressive reduction of their summed moment and therefore a decline in their dipole contribution. Between 1900 and 1990 the Earth's dipole moment reduced from 8.29 to 7.84 10^{22} Am^2 ([dataset]* GFZ, 2025), which is therefore attributable to the NA-SA induction pair weakening. This weakening was accompanied by a dramatic North Magnetic Pole (NMP) shift: between 1900 and 2020 the NMP moved from a position near the NA SWIC circuit center in 1900 to its current position near to the geographic north pole, that is to an intermediate position between the NA and EA SWIC circuit centers along a path connectin g the two (Fig. 14). The two possible causes of the NA-SA inductor pair weakening are:

- temperature increases along the NA circuit periphery are causing its "normal" moment to decrease
- temperature decreases along the SA periphery are causing its "reverse" moment to increase.

Since 1900 there have been 13 Large (VEI ≥ 5) volcano eruptions ([dataset] Global Volcanism Program, 2024), 4+1 along the NA periphery (Santa Maria, Novarupta, Mt St Helens, El Chichón; plus 1 in the Kurils, Kharimkotan), 3 along the SA periphery (Cerro Hudson, Cerro Azul, Puyehue-Cordon Caulle), 3 along the EA periphery (Ksudach, Bezymianny, Pinatubo), and 2 along the O periphery (Agung, Hunga Tonga). This suggests that the NA and SA circuits are heating relative to the EA and O circuits, and that the "normal" NA circuit magnetic moment is decreasing faster than its "reverse" magnetic moment SA counterpart.

The current NA to EA NMP migration began in 1859, the year of the largest magnetic storm on record, a coronal mass ejection known as the Carrington Event (BGS, 2025b). It is extremely unlikely that the two events are unrelated, as the Carrington event's geomagnetic field deformation of up to -1750 nT is orders of magnitude larger than the ~-50 nT Solar Quiet deformation caused by a 5 TW solar wind (Fig. 4). The Event therefore generated relatively huge amounts of EM flux, which in turn must have induced significant currents and heating in all the SWIC circuits, energy which apparently disrupted the pre-1859 relative strengthening of the NA-SA inductor pair. The NMP was travelling southward at an average speed of 1.2 km/a between 1849-1859, but in 1859 suddenly reversed to an average northward speed of 3.7 km/a the following decade (Fig. 14). Note that 3 of the 4 post-1750 VEI 6 volcanoes occurred between 24 (Krakatoa) and 53 (Novarupta) years after the Carrington event, CMB-to-surface time lags that are similar to the Maunder volcanism following the post-Spörer heating.

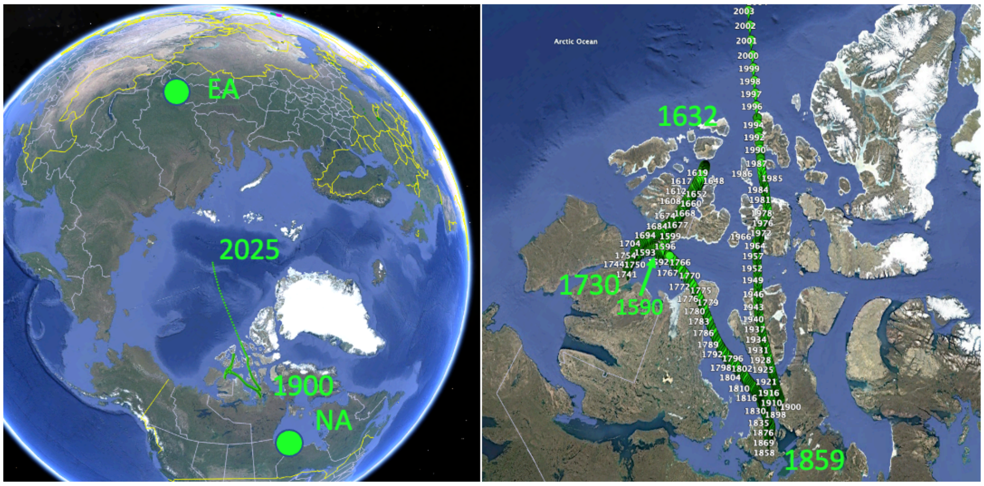

Figure 14: © Google Earth view of the North Magnetic Pole positions between 1590 and 2025. ([dataset]* NOAA 2025); large green dots are the locations of SWIC circuit centers

In contrast a more typical minor NMP movement reversal occurred around 1632, when the NMP was travelling northward towards the EA center at a gradually declining average speed of 14 km/a (1590-1600) to 11 km/a (1600-1610) to 7.5 km/a (1610-1620) to 2 km/a (1620-1630) to a virtual standstill between 1630-1633 ([dataset]* NOAA 2025). Figures 13 and 14 (right) suggest that between 1590-1633 the EA-O inductor pair was progressively weakening due to circuit heat increases, and that the NA circuit was relatively cool and strengthening (no large volcanoes). The total geomagnetic dipole moment was increasing over the 1624 – 1717 period, which was most likely the result of a decreasing (reverse) strength of the SA circuit due to pre-Maunder warming. The high levels of volcanic activity during the Maunder Minimum (Figure 13; left) are mainly attributable to the pre-Maunder heating of the O, EA, and SA circuit peripheries (Fig. 13 right). Three of the seven VEI 6 volcanoes (Billy Mitchell, Huaynaputina, Long Island) of the last 500 years occurred during the Maunder minimum, 3 of seven occurred within 53 years of the Carrington event; the last, Pinatubo (1991), could plausibly be due to the most recent 100-year solar maximum SWIC circuit heating around ~1950.

Some of the earliest scientific observations suggest a large shift / minor geomagnetic excursion happened between 900-1100: Chinese scientists observed an increase in magnetic declination from -15° in 900 to 15° in 1100 (Smith & Needham, 1967;

note: declination sign reversed in order to be consistent to the CALS7K.2 model), and so documented an NMP movement from near the EA circuit center to its NA counterpart. This shift is also very apparent in the Paris paleomagnetic declination data (Gallet et al., 2003) as well as CALS7K.2 declination animations (https://earthref.org/ERDA/432/ accessed 2025 June 24). This shift coincided with a dipole moment increase (Fig. 12), which is likely not fortuitous given that both phenomena can be attributed to coupled inductor pair strength variations: the NMP shift and the increase in dipole strength are both consistent with a relative strengthening of the NA-SA pair over the period. A speculative explanation is therefore that similar to the Maunder Minimum, during the solar maximum prior to the Oort minimum (Fig. 12) the SA circuit heating caused the SA circuit reverse moment to decrease, leading to a NA-SA paired inductor dipole moment increase during the Oort minimum, thereby causing the NMP movement towards the NA circuit center.

5.5 The Geomagnetic Power Spectrum

Numerous authors have recognized solar signatures in the geomagnetic power spectrum: the 21.4 year cycle (2 solar reversals; Currie, 1973), the yearly and twice yearly cycles (Banks, 1969), the 27 day cycle (related to the solar rotation period; Banks, 1969), and the daily cycle (Fig. 4) all show significant power spectrum peaks that occur on a worldwide scale, indicating they all likely represent the Earth's global magnetic response to incident solar wind strength variations.

Banks (1969) theorized that the ratio of the external to internal parts of the geomagnetic field at the Earth's surface is dependent on both the external energy source as well as Earth's magnetic response, and determined that a P_1^0 spherical harmonic is an adequate representation of the latitude dependency of the geomagnetic field at the Earth's surface for solar cycles between 0.5 cycles/day and 2 cycles/year. The twice-yearly signal has a frequency of 10^{-7} Hz, which is a deep-Earth response even under Banks' (static) skin depth model. The P_1^0 spherical harmonic is the simplest sectoral harmonic, and signifies that for these low frequency solar cycles Earth's internal response is latitude-invariant, and is highly similar to its diurnal response. This is entirely consistent with the Geo-SWIED model, as the longitudinal position of the Sun at LT 12:00 determines paired SWIC inductor strength, not the latitude, so a P_1^0 Earth response is both expected and observed. The fact that all cycles between 0.5 cycles/day and 2 cycles/year show a similar response indicates that all the higher-frequency cycles between 10^{-7} and 10^{-5} Hz are likely due the OC's diurnal induction response to the SWICs. The lower cycles, for example the 27-day cycle, can be seen as multiples of the daily 10^{-5} Hz cycle.

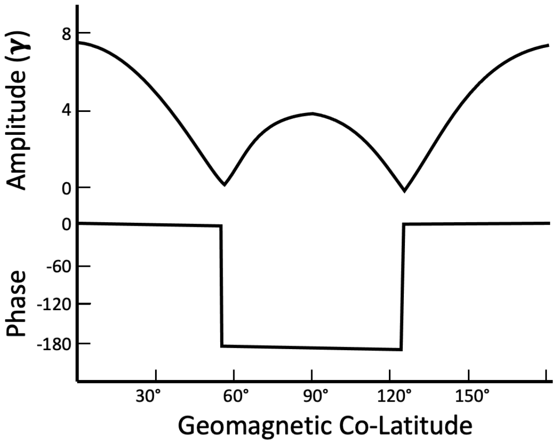

Figure 15: Latitude dependence of the annual vertical (radial) field variation: best least squares fit of Banks' (1969) P_0^2 model

Banks' (1969) study also determined that the annual power spectrum line was better modelled by a P_2^0 spherical harmonic, a tesseral harmonic that is entirely consistent with the yearly response of the Geo-SWIED model. Figure 15 presents the latitude dependency of the vertical (radial) component of Banks' (1969) P_2^0 model, and demonstrates the similarity of Earth's geomagnetic response for the high latitudes (55-90°N/S), which is very likely due to the shifting of the NH and SH high-latitude large magnetic flux locations ("sweet spots") with the seasons. The Tropic of Cancer (~23° N)/ Capricorn (~23° S) are the most northern / southern circles of latitude resp. at which the sun is directly overhead at the June / December solstice. When the Sun is directly over the Tropic of Cancer, the SH polar area – and the SH high-latitude flux sweet-spots – have shifted almost entirely to the magnetotail side of the magnetosphere: the entire Antarctic circle is on Earth's dark, leeward side, so less SH high-latitude geomagnetic flux is generated, resulting in reduced SH SWIC strengths. It is also by no means coincidental that the 4 main SWIC loop centers lie roughly at 55° N/S, the boundary between the relatively productive (55-90°N, 55-90°S) and non-productive, low-angle geomagnetic inclination areas in between.

5.6 Geo-SWIED: Secular westward drift of the non-dipole field

For the past 150+ years (since the Carrington event) the non-dipole field has been shifting westward at an average rate of 0.18°/a (Merrill et al., 1998). This westward shift is easily explainable under the Geo-SWIED model: under the current "normal" polarity the SWICs run clockwise (when viewed from the north) around their circuits, and are therefore strongest in their east but lose energy due to Ohmic heat losses as they circuit to the west. This relatively large heating of the eastern circuit boundary over time results in a migration of the SWIC path – and its resultant non-dipole - to a cooler, lower-resistivity paths to the west (Fig. 15).

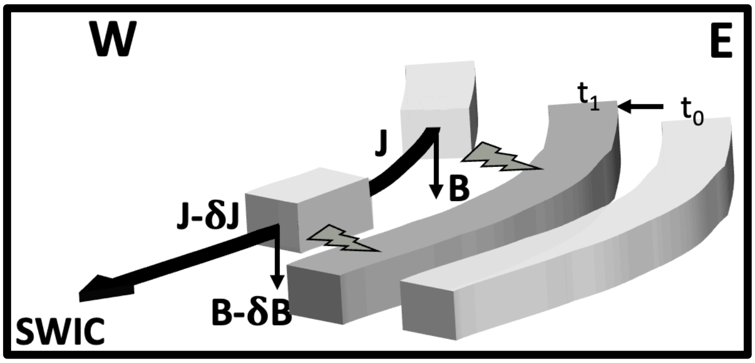

Figure 16: schematic of a "normal" polarity SWIC circuit, running along the CMB, and contained by heat barriers (grey curved beams to the E). Along its pathway the SWIC loses strength (**δ**J) due to Ohmic heat losses resulting in a westwardly / inwardly shift of the SWIC over time (t_0 -> t_1) as well as a loss of induced field strength (**δ**B).

It is interesting in this regard that paleomagnetic declination data measured in Paris and modelled by CALS7K.2 (Gallet et al., 2003) demonstrate the eastward secular drifts of the magnetic pole between 900-1400 and 1600-1800 that roughly concur with dipole moment strengthening and OC cooling, while the westward secular NMP drifts between 1400-1600 and 1800-present correspond to dipole moment weakening and OC warming.

5.7 Geomagnetic Strength of a SWIC inductor loop

A SWIC circuit's magnetogenic efficiency was estimated to be 0.33: the ~5 TW of solar wind power that reaches the OC roughly creates 3.3 TW of heat and 1.7 TW of magnetic power. A SWIC circuit's radius varies (Fig. 6,9): the surface trace of the EA circuit increases from around 4500 km to the East, to 6500 km in the west. Note that these radii need to be scaled / projected down to the CMB. For the following calculations an average surface radius of 5500 km, corresponding to an OC circular SWIC radius, R, of 2900 km are assumed (~ 0.85 * $R_{OC'}$). Further assuming a (highly uncertain) core conductivity of 6 x 10^5 S.m^{-1} (resistivity of 1.67 x 10^{-6} Ω.m; Merrill et al., 1998), and magnetic permeability of μ_C of 1.0 x 10^{-3} N.A^{-2} (Ott, 2009), the EA SWIC current, I, can be estimated (Ohm's Law):

$$I = \sqrt{\frac{P}{R}} = \sqrt{\frac{(1.7)\,10^{12}\,W}{1.67\,10^{-6}\Omega.\mathrm{m}*2*\pi*2.9\,10^{6}m}} \approx 236\;kA \qquad \text{(Eqn. 9)}$$

Its magnetic field strength, B_{avg}, can be estimated using the Biot-Savart law (Purcell & Morin, 2013):

$$B_{avg} = \frac{\mu_C I}{2R} = \frac{1\,10^{-3}\left(\frac{N}{A^2}\right)(2.4)\,10^{5}\,A}{2*3\,10^{6}\,m} \approx 40\;\mu T \qquad \text{(Eqn. 10)}$$

Note that this is a surprisingly accurate estimate of Earth's average field strength given the large uncertainties.

6 Other planets

The SWIED framework can be used to clarify the "problematic" magnetic field geometries and heat anomalies of other planets, and to hindcast their magnetic field strengths.

6.1 Planetary Magnetic Field Strength

Using the work-energy principle, Dessler (1974) calculates Earth-incident solar wind power, U_s, as:

$$U_s = \pi\, R_M^2 \left(\frac{1}{2}\rho V_s^2 + \frac{B_{IMF}{}^2}{2\mu_0}\right) V_s \approx 5\, TW \qquad \text{(Eqn. 11)}$$

where (assumed values between brackets) R_M is the magnetosphere radius (12 Earth radii), ρ the mass density of the solar wind (8.10^{-21} kg.m^{-3}), Vs the solar wind velocity (400 km/s), B_{IMF} the strength of the interplanetary magnetic field (10 nT), and μ_0 the vacuum magnetic permeability (1.26 10^{-6} H/m). Note that the second term between the round brackets, the incident magnetic energy of the IMF, is commonly ignored as its size is much smaller than the first term, which represents the solar wind momentum energy.

Planet	Radius (R)			Solar Wind					
	Planet (Mm)	R_M/R_P	Core (Mm)	ρ amu/cm^{-3}	Vs m/s	P TW	I kA	B_{calc} µT	B_o µT
Mercury	2439	1.5	1951	60	500	0.16	55	**16.6**	**0.2**
Earth	6378	10	3441	8	500	6.4	263	**45**	**30.6**
Jupiter	71398	46	3570	0.3	500	635.4	2579	**425**	**430**
Saturn	60330	20	9050	0.1	500	28.6	344	**22.3**	**21.4**
Uranus	25559	25	3323	0.02	500	1.6	134	**23.8**	**22.8**
Neptune	24764	24	3715	0.008	500	0.6	75	**11.8**	**14.2**

Table 1: Comparison of Predicted (B_{calc}) versus Observed (B_o) Surface Equatorial Magnetic Field strength for 6 planets. ρ: density, V: velocity, P: power, I: current intensity

Table 1 presents the parameters that were used for the planet field strength calculations. Sources:

- solar wind & magnetosphere parameters (Table 7.1 in Kivelson & Bagenal, 2014)
- the planets' ferromagnetic core radii: Marley & Fortney, 2014 (gas and ice giants, Fig. 33.7 & 33.9), Murchie et al., 2014 (Mercury) and Merrill et al., 1998 (Earth).
- Magnetogenic efficiency (0.33), core resistivity (1.67 x 10^{-6} Ω.m), magnetic permeability (1.0 x 10^{-3} N.A^{-2}), and planetary SWIC circuit radius (0.85 * Rcore) are treated similar / analogous to Earth.

Eqn. 11 was used to first calculate the planet-incident solar wind power, P (Table 1). Eqns. 9 & 10 were then used to calculate the individual planet SWIC intensities (I) and equatorial magnetic field strength (B_{avg}) under assumptions identical to the previous section. Mantle energy absorption was ignored.

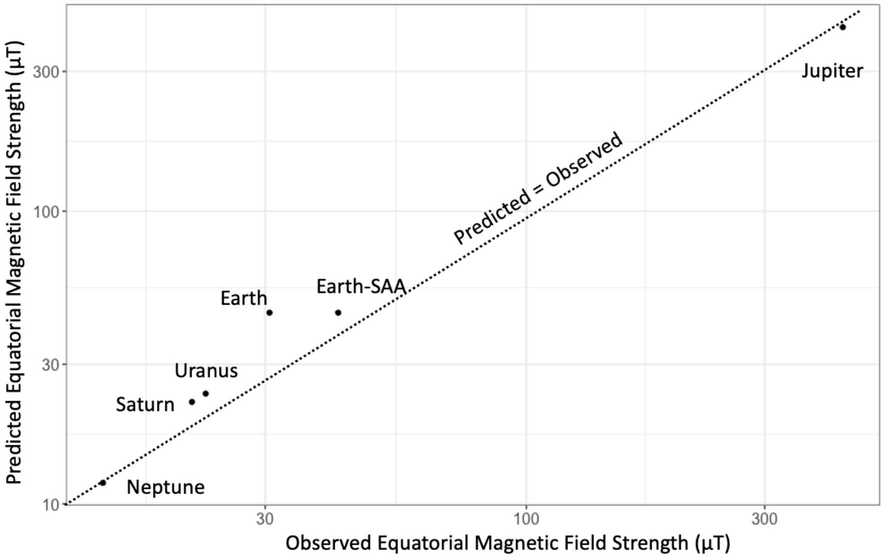

Figure 17: SWIED-predicted versus observed planetary equatorial magnetic field strength. Mercury (x=0.2; y=16.5) is not plotted. Note: logarithmic axes

The method provides a remarkably good fit for the gas and ice giants (Fig. 17), a reasonable fit for Earth, and a very poor fit for Mercury (not displayed). Fig. 17 clearly demonstrates that the SWIED physical model has predictive power, and that most planetary magnetic field strengths have a strong correlation with average incident solar wind energy. Some comments:

- If both of Earth's mid-latitude SWIC circuit pairs had been constructively interacting (e.g. EA-O) rather than one pair destructively interacting (NA-SA), Earth's fit ("Earth-SAA" in Fig. 17) is much better: the observed magnetic field strength in Singapore (~42 µT) better matches the predicted equatorial value than that of Quito (~28µT).
- The method is unsuitable for Mercury. Mercury has a 3:2 resonance orbit around the Sun (Dehant and Van Hoolst, 2014), whereby the same side of the planet is facing the Sun for prolonged periods of time, and a sideral rotation period of 58.65 Earth days (Murchie et al., 2014): a Mercury solar day lasts 176 Earth days, thereby significantly limiting its diurnal solar wind generated magnetic flux. It also has a very thin Mantle, and a core which comprises the bulk of the planet (Murchie et al., 2014). In addition, the Sun occasionally "backtracks" through Mercury's sky (Murchie et al., 2014), indicating Mercury is unique in its SWIC generation. Mercury's weak field is also problematic under kinematic dynamo theory (Stanley, 2014).

6.2 Two problematic planetary magnetic fields and their heat anomalies

The SWIED model explains the great similarity (in essence more similar than dissimilar) between the magnetic fields of the planets: a highly conductive ferromagnetic core, a low magnetically permeable non-ferromagnetic mantle, and significant diurnal EM flux energy generated during a planet's rotation around its axis are the only requirements for a planetary magnetic field, which is the reason why most planets have one. Planets with longer orbits (Neptune, Uranus) show asymmetric magnetic fields and heat anomalies, as their summer hemispheres experience extended solar wind exposure, causing prolonged contrasts in NH and SH SWIC strengths and overlying heat anomalies. The variability in the length of the planetary solar days and years, solar distance, rotational axes tilts, and planetary core radii therefore largely explain the variability of the planetary magnetic field geometries and strengths, as well as their heat anomaly geometries.

6.2.1 Saturn's Field

Both Saturn's magnetic field geometry and its heat anomalies are enigmatic. Saturn's magnetic field geometry cannot be explained under kinematic dynamo theory (Cowling, 1955; Kivelson & Bagenal, 2014), as its axisymmetric field geometry can only be modeled under numerous very large and unsubstantiated assumptions (Kaiser & Tilgner, 2014). In contrast, an axisymmetric field is the most easily-explained, basic geometry under a SWIED model. If Fig. 8 had represented a mid-latitude quadrupole on Saturn, whereby a constant total amount of positive (Saturn has reverse polarity) solar wind generated flux entered Saturn's ferromagnetic core at NH and SH high-latitudes, then the quadrupole's paired SWIC circuits would generate a perfectly axisymmetric reverse polarity field.

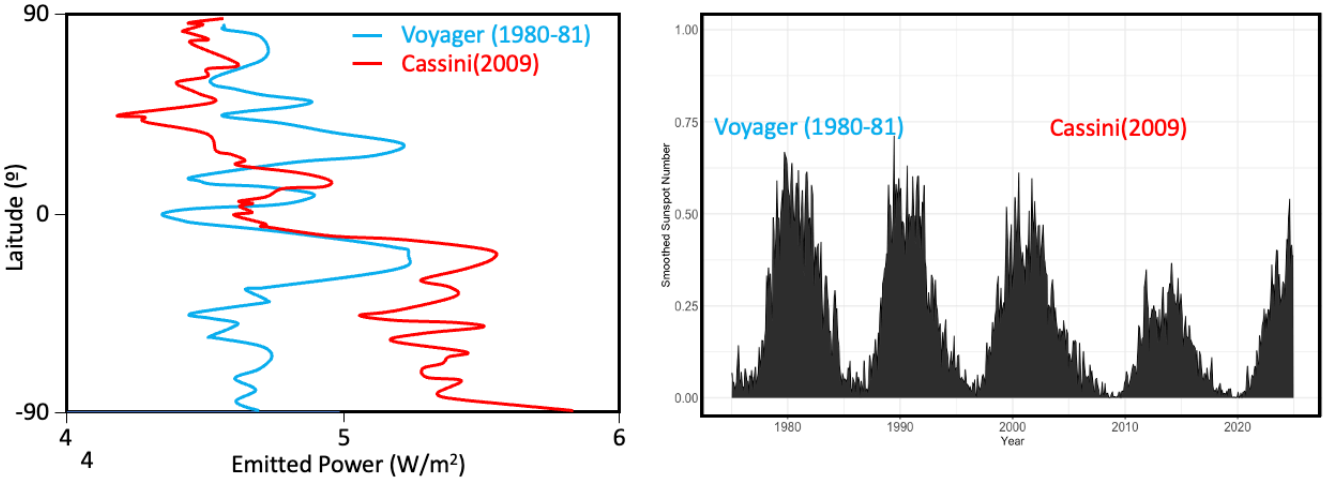

Figure 18: (left) Comparison of the meridional distribution of emitted power between the Voyager (November 1980 – August 1981) and Cassini (up to 2009) missions (After Li et al., 2010). (right) Earth-measured sunspot count, a proxy for solar activity [dataset]* WDC-SILSO

https://doi.org/10.5194/egusphere-2025-3454
Preprint. Discussion started: 6 August 2025

Similar to all Gas and Ice Giants, Saturn's heat budget must rely on an obscure internal energy source to explain why it emits more thermal energy than it receives through solar irradiation (Wang et al., 2025; Irwin et al., 2025): Saturn radiates twice the energy it receives from solar irradiation (Li et al., 2010), and requires an extra 2.5 TW of heating power per hemisphere to explain observed temperatures (Cowley et al., 2004). Observations preclude most internal heat source candidates:

- Saturn emitted less energy each year from 2005 to 2009 (Li et al., 2010). Its effective NH temperature dropped between 2005 to 2008 but started to warm up again by 2009 during the run-up to its summer (Li et al., 2010).
- In 2010 Saturn's heat radiation was asymmetrical: its southern hemisphere radiated about one-sixth more energy than its northern one (Fig. 18, red line; Li et al., 2010). During the Voyager mission, roughly 1 Saturn year earlier, the two were more in balance, indicating solar irradiation is almost certainly not responsible for the variations.
- Saturn's heat anomalies continually varied with its seasons, mirroring the expected hemispherical temperature shifts: an equatorial heat anomaly during the 1997 equinox migrated to the south pole in 2006 during the SH's summer, after which it migrated to the north, causing northern hemisphere heat anomalies, and finally ended at Saturn's north pole by its 2017 NH summer (Fletcher et al., 2023).
- The Cassini mission demonstrated some unforeseen and enigmatic interannual variability. One Saturn year (29.4 Earth years) after the Voyager measurements, a comparison of the two meridional distributions of emitted power (Fig. 18 left) indicates significant differences, and strongly suggests a Saturn-internal power source is at work (Li et al., 2010).

Formational heat or "helium rain" accreting at the core are therefore unlikely causes, as neither would show such interannual or regional variability. In addition, Kelvin-Helmholtz modeling indicates Saturn lost its formational heat over 2 billion years ago (Marley and Fortney, 2014). Saturn's heat anomalies are broadly consistent with its seasonal changes, strongly suggesting a solar energy source is almost certainly responsible: the NH warmed and the SH cooled during its transition to northern summer between its 2009 (equinox) and 2017 (northern summer solstice). Its 2017 NH polar heat anomaly, however is difficult to explain, as its poles are more distant to the sun than its equator, and its north pole solar irradiance incidence angles are lower: the poles receive less net solar energy than the equator or the mid-latitudes. Solar wind is the only other solar power reaching Saturn, and fortunately fits the observations very well:

- The 5 TW of power Crowley et al. (2004) indicated are required for Saturn's higher thermosphere temperature represents roughly 18% of the 28 TW of estimated Saturn-incident solar wind power (Table 1), so the incident solar wind is a credible power source for both Saturn's magnetic field, energy crisis, and its enigmatic climate forcing.
- Saturn's SWIC circuits could resemble a quadrupole such as those in Fig. 8 though the hexagonal shape of its north pole heat anomaly (Fletcher et al., 2023) suggests a hexapole may be more likely. Saturn's paired SWIC circuits pass near the poles, that is near the high-latitude areas of large diurnal solar wind generated EM flux, and near to the equator, where their NH and SH circuits' toroidal induced fields repel and heat each other.

- The difference between the Voyager and Cassini missions can largely be attributed to differences in solar wind strength (Fig. 18, right): Voyager visited during the solar (wind) cycle 21 maximum, while the Li et al., 2010 data (declining temperatures between 2005 – 2009) were recorded during the waning days of solar cycle 23 (see also below), which was characterized by a long, complex solar minimum with very low solar wind values (Zerbo and Richardson, 2015). The Cassini mission therefore documents a period during which the solar wind contribution to Saturn's emitted heat was smaller.

6.2.2 Neptune's Field

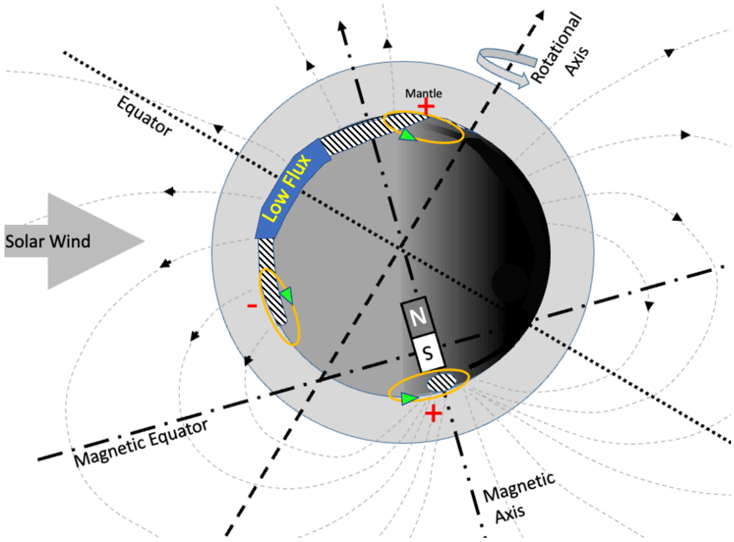

Fig. 19: Schematic of Neptune's magnetic field (after Ness et al., 1989). Thin dashed lines represent magnetic field lines; thick dashed line the rotational axis; dot-dash line the magnetic equator. Solid orange ovals with green arrows indicate SWIC circuits. Hatched areas represent sun-side high inclination "sweet spot" areas. Red plus / negative signs indicate solar wind generated EM flux.

Neptune's magnetic and heat anomalies show a great deal of similarity with Saturn's (Connerny et al., 1991; Pearl & Conrath, 1991; Stanley & Bloxham, 2004; Roman et al., 2020):

- Neptune's magnetic field cannot be explained under kinematic dynamo theory. Credible high $\mu\sigma$ kinematic dynamo source layers and Neptune-internal energy sources are absent.
- Enigmatic processes are causing heat anomalies in Neptune's atmosphere on subseasonal timescales, and on both regional and global scales
- Neptune's global thermal emissions declined between 2003 and 2010.

- Neptune's SH heat anomaly peaked during its summer solstice; its south pole temperature was warmest between 2003 and 2006, decreased thereafter, but increased abruptly again in 2018.

Neptune radiates around 2.6 times the heat energy that it receives from high-frequency solar radiation (Pearl & Conrath, 1991), which strongly implies that - similar to Saturn – the solar wind is increasing Neptune's internal energy. Neptune's magnetic field (Fig. 19) can be modelled as a magnetic dipole that shows a relatively large tilt of 47°, and is offset by a relatively large amount of 0.55 R_N (13500 km) from its center (Ness et al., 1989). Neptune's year lasts 165 Earth years (Roman et al., 2022) indicating Neptune's seasons last over 41 years. Its southern summer solstice was in 2005 (Roman et al., 2022), so Neptune had just entered its SH summer at the time of the Voyager 2 flyby in 1989.

Figure 19 demonstrates that the SWIED model easily explains both Neptune's complex magnetic field geometry as well as its surface heat anomalies. The solar wind cannot compress magnetic field lines that are parallel to it (Eqn. 4), resulting in a "Low Flux" area (Fig. 19) near its equator on the dayside of the planet. It does however deform anti-parallel field lines to the north and south of this zone. Under its current magnetic field geometry (Fig. 19) this compression results in two positive EM flux patches (B_{SH} and B_{NH} in Fig. 20), where the solar wind "pushes" more field lines (positive flux) into these sweet spots, and one negative EM flux patch (B_{SSH}), a second SH flux patch (SSH), where the solar wind pushes field lines out of the sweet spot. Most of the solar wind generated positive EM flux enters Neptune in the SH, causing a powerful SH SWIC circuit, whose center lies at ~30ºS. In contrast, its NH sweet-spot is very broad, has relatively low magnetic flux density, and therefore receives less EM flux, causing a weaker NH SWIC circuit at a relatively higher (~55º N) latitude. The SSH SWIC circuit, is mainly noticeable as a SH non-dipole anomaly (Fig. 20). These 3 flux patches generate a non-axial reverse quasi-dipole (tripole) magnetic field (Fig. 20) characterized by two "reverse" magnetic moments (B_{SH} and B_{NH}), that constructively generate a non-axial offset dipole, and one "normal" magnetic moment (B_{SSH}) that further pulls the dipole off-axis (Fig. 20). The calculated tripole moment results in the (observed) 47° dipole tilt (Ness et al., 1989).

Similar to Saturn, Neptune cooled between 2003 to 2009 (Roman et al., 2022), likely due to the waning of the solar wind at the end of solar cycle 23. Eqn. 11 varies as the cube of solar wind strength, so a very high solar wind velocity of 800 m/s (Zerbo & Richardson, 2015) during active solar periods transfers sixty four times more power to Neptune (2.3 TW) than a very low velocity, low solar activity wind of 200 m/s. This explains why the SH thermal emissions peaked during the summer solstice in 2005, at the maximum of solar cycle 23 (Fig. 18 right), why its south pole temperature was highest between 2003 to 2006, and why the south pole temperature decreased thereafter during the solar cycle 23 minimum in 2008. The SH and south pole temperatures very likely increased again around 2013, in the run-up to the solar cycle 24 maximum (unfortunately a 2013 – 2017 data gap exists in the Roman et al., 2020 dataset), though in 2018 solar activity was almost certainly higher than in 2008.

https://doi.org/10.5194/egusphere-2025-3454
Preprint. Discussion started: 6 August 2025

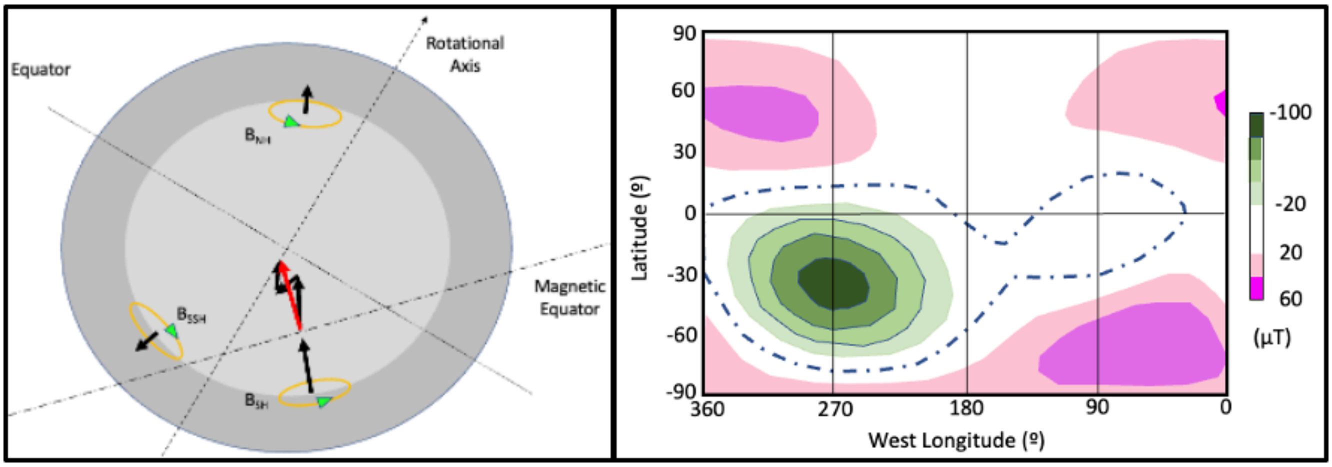

Fig. 20: (left) Same as Fig. 19, but with induced magnetic moments added (black arrows) as well as their summed magnetic moment (red arrow); (right) Neptune surface radial magnetic fields. Dot-dash line is the magnetic equator (After: Connerny et al., 1991)

The SWIED model predicts significant heating occurs where the SWICs are strongest: the high latitude south pole has a lower angular velocity than the ~30º S SWIC center, so will heat relatively longer during a Neptune day. Observations indicate Neptune's south pole temperature roughly peaked in 2018 (Roman et al., 2022), that is roughly during the solar cycle 24 maximum (2012-2018 data missing from the Roman et al. dataset). Note that the SWIED model predicts that Neptune's magnetic field and heat anomalies will very likely be inverted during its northern summer in 2087.

4 Summary

The Solar Wind Induced Electric Dynamo (SWIED) model explains the presence, magnitude, geometry and stability of the Earth's dipolar and non-dipolar fields, as well as its current polarity. It clarifies the origins of Earth's fluid Outer and solid Inner Core, and offers realistic mechanisms for geomagnetic excursions and reversals, secular non-dipole drift, and solar signals in the geomagnetic power spectrum. It accounts for the areas of high surface heat flow that originate in the Outer Core, thereby establishing a credible link between magnetogenesis, volcanism and continental drift.

The Gas and Ice Giants' magnetic fields are very likely generated by similar SWIEDs, whose by-product is substantial waste heat that significantly contributes to emitted planetary heat, largely explaining why these planets emit more energy than they receive via solar irradiation alone. The SWIED model rationalizes their magnetic field geometries and heat anomalies, and accurately predicts their magnetic field strengths from best-estimate input data.

Methods:

The plots were created in R, and Google Earth.

Data Accessibility

[dataset]* GFZ (Deutsches Geoforschungszentrum), 2025: Historical Geomagnetic Dipole moment CALS10k. https://www.gfz-potsdam.de/fileadmin/gfz/sec23/data/Models/CALSxK/DM_CALS10k_2.zip. Retrieved 2025-06-20.

[dataset]* Global Volcanism Program, 2024. [Database] Volcanoes of the World (v. 5.2.8; 6 May 2025). Distributed by Smithsonian Institution, compiled by Venzke, E. https://doi.org/10.5479/si.GVP.VOTW5-2024.5.2

[dataset]* NOAA, Wandering of the Geomagnetic Poles, https://www.ngdc.noaa.gov/geomag/data/poles/NP.xy; Retrieved 2025-06-20

[dataset]* WDC-SILSO, Royal Observatory of Belgium, Brussels, DOI: https://doi.org/10.24414/qnza-ac80". Retrieved 2025-06-20

References

Aubert, J., 2020, Recent geomagnetic variations and the force balance in Earth's core, *Geophysical Journal International*, **221**, 378–393, https://doi.org/10.1093/gji/ggaa007

Baker, D., Pulkkinen, T., Hesse, M., McPherron, R., 1997, A quantitative assessment of energy storage and release in the Earth's magnetotail. *JGR*, **102**, 7159-7168, doi: 10.1029/96JA03961.

Banks R.J., 1969, Geomagnetic Variations and the Electrical Conductivity of the Upper Mantle, *Geophys. J. R. Astr. Soc.*, **17**, 457-487.

BGS (British Geological Survey), 2025a, The Earth's magnetic field: an overview. http://www.geomagnetism.bgs.ac.uk/education/earthmag.html Downloaded 24-06-2025

BGS (British Geological Survey) 2025b, The Largest Magnetic Storm on Record...or is it? http://www.geomag.bgs.ac.uk/education/carrington.html, Downloaded 24-06-2025

Burke K., 2011, Plate Tectonics, the Wilson Cycle, and Mantle Plumes: Geodynamics from the Top. *Annu. Rev. Earth Planet. Sci*., **39**, 1–29, doi: 10.1146/annurev-earth-040809-152521

Collins, G., Johnson J., 2014, Ganymede and Callisto. *In: Encyclopedia of the Solar System (Third Edition), Academic Press*, ISBN: 978-0-12-415845-0, p. 813-829

Connerny, J., Acuna, M., Hess, N., 1991, The Magnetic Field of Neptune., *JGR*, **96**, 19023-19042

Coro, G., Trumpy, E., 2020, Predicting geographical suitability of geothermal power plants, *Journal of Cleaner Production*, **267**, 121874, doi: https://doi.org/10.1016/j.jclepro.2020.121874.

Cowley, S., Bunce, E., and O'Rourke, J., 2004, A simple quantitative model of plasma flows and currents in Saturn's polar ionosphere, *J. Geophys. Res.*, 109, A05212, doi:10.1029/2003JA010375.

Cowling, T.G., 1955, Dynamo theories of cosmic magnetic fields, *Vistas in Astronomy*, **1**, 313-322, https://doi.org/10.1016/0083-6656(55)90041-6.

Crooker, N., Feynman, J., Gosling J. T., 1977, On the high correlation between long-term averages of solar wind speed and geomagnetic activity. *JGR,* **82**, 1933. doi:10.1029/JA082i013p01933

Currie, R.G., 1973, Geomagnetic line spectra-2 to 70 years. *Astrophys Space Sci,* **21**, 425–438, doi: 10.1007/BF00643106

De Michelis, P., Tozzi, R., Meloni, A., 2005, Geomagnetic jerks: observation and theoretical modeling. *Memorie della Società Astronomica Italiana*, **76,** 957–960

Dehant, V., Van Hoolst T., 2014, Rotation of Planets. *In: Encyclopedia of the Solar System (Third Edition), Academic Press.* ISBN: 978-0-12-415845-0, p 159-184

Dessler A., 1974, Some Problems in Coupling Solar Activity to Meteorological Phenomena. *Symp. Possible Relationships between Solar Activity and Meteorological Phenomena, Nov. 1973, NASA*., 187-197

Eddy J., 1976, The Maunder Minimum. *Science*, **192**, 1189-1202

Ekström, G., Dziewonski, A.M., 1998, The unique anisotropy of the Pacific upper mantle. *Nature,* **394**: 168–172

Fletcher, L, Sromovsky, L., Hue, V., et al., 2023, Saturn's Seasonal Atmosphere at Northern Summer Solstice, arXiv:2012.09288v3 , https://doi.org/10.48550/arXiv.2012.09288

Gallet, Y., Genevey, A., Courtillot, V., 2003, On possible occurrence of 'archaeomagnetic jerks' in the geomagnetic field over the past three millennia. *Earth and Planetary Science Letters,* **214**, 237-242, doi:10.1016/S0012-821X(03)00362-5.

Gosling J.T., 2014, The Solar Wind. *In: Encyclopedia of the Solar System (Third Edition), Academic Press* ISBN: 978-0-12-415845-0, p.261-279

Gubbins D., 1999, The Distinction between Geomagnetic Excursions and Reversals. *Geophys. J. Int*, **137**, F1-F3, https://doi.org/10.1046/j.1365-246x.1999.00810.x

Gubbins D., Love, J., 1998, Preferred VGP paths during geomagnetic polarity reversals: Symmetry considerations. *Geophysical Research Letters*, **25**, 1079–1082. doi:10.1029/98GL00711

Gubbins D., Alfè, D., Masters, G., Price, G., Gillan, M.J., 2003, Can the Earth's dynamo run on heat alone?. *Geophysical Journal International*, **155**: 609-622. doi://doi.org/10.1046/j.1365-246X.2003.02064.x

Hamza, V. M., Cardoso, R. R., Ponte Neto, C. F., 2007, Spherical harmonic analysis of Earth's conductive heat flow. *Int J Earth Sci*, **97**, 205-226, doi: 10.1007/s00531-007-0254-3

Herman, J., Goldberg R., 1978, Sun, weather, and climate. *Scientific and Technical Information Office, NASA*

Isshiki, M., Igaki, K., 1978, Temperature Dependence of the Electrical Resistivity of Pure Iron at Low Temperatures, Transactions of the Japan Institute of Metals, **19**, 431-437, https://doi.org/10.2320/matertrans1960.19.431

Irwin, P.G.J., Wenkert, D.D., Simon, A.A., et al., 2025, The bolometric Bond albedo and energy balance of Uranus, https://doi.org/10.48550/arXiv.2502.18971

Kaiser, R., and Tilgner, A., 2014, The axisymmetric antidynamo theorem revisited. *SIAM Journal on Applied Mathematics*, **74,** 571-597. DOI:10.1137/130928376

Khurana, K.K., Kivelson, M.G., Stevenson, D.J., Schubert, G., Russell, C.T., Walker, R.J., & Polanskey, C.A., 1998, Induced magnetic fields as evidence for subsurface oceans in Europa and Callisto. *Nature,* **395**,777-780.

Kivelson, M. G., Khurana, K.K., Russell, C.T., Volwerk, M., Walker, R.J., Zimmer, C., 2000, Galileo Magnetometer Measurements: A Stronger Case for a Subsurface Ocean at Europa. *Science*, **289**, 1340-1343

Kivelson, M.G., Bagenal, F., 2014, Planetary Magnetospheres *In: Encyclopedia of the Solar System (Third Edition), Academic Press*; ISBN: 978-0-12-415845-0, p. 137-157

Kushinov, A.V., 2008, 3-D Global Induction in the Oceans and Solid Earth: Recent Progress in Modeling Magnetic and Electric Fields from Sources of Magnetospheric, Ionospheric and Oceanic Origin. *Surv Geophys,* **29**, 139–186. https://doi.org/10.1007/s10712-008-9045-z

Li, L., Conrath, B., Gierasch, P., et al., 2010, Saturn's emitted power, *J. Geophys. Res.*, 115, E11002, doi:10.1029/2010JE003631.

Lühr, H., 2000, CHAMP Magnetic Field Recovery. http://op.gfz-potsdam.de/champ/science/magnetic_SCIENCE.html Retrieved 16 August, 2021

Marley, M.S., Fortney, J.J., 2014, Interiors of the Giant Planets. *In: Encyclopedia of the Solar System (Third Edition), Academic Press*, 743-758, ISBN: 978-0-12-415845-0

Matsushita, S. Maeda H., 1965, On the geomagnetic solar quiet daily variation field during the IGY. *JGR*. **70**, 2535–2558, doi: 10.1029/JZ070i011p02535

McFadden, P., Merrill, R.T., 1995, Fundamental transitions in the geodynamo as suggested by paleomagnetic data, *Physics of the Earth and Planetary Interiors*, **91**, Pages 253-260, doi: 10.1016/0031-9201(95)03030-Z.

Merrill, R.T., McElhinny, M. W., McFadden, P. L., 1998, The magnetic field of the earth: paleomagnetism, the core, and the deep mantle. Academic Press. ISBN 978-0-12-491246-5.

Morelli, A., 2007, Core Mantle Boundary topography, seismology, *In: Encyclopedia of Geomagnetism and Paleomagnetism, Academic Press*, Springer Nature, Gubbins, D. and Herrero-Bervera, E. (Eds.), pp 125-127

Murakami, M., Goncharov, A., Miyajima, N., et al., 2022, Radiative thermal conductivity of single-crystal bridgmanite at the core-mantle boundary with implications for thermal evolution of the Earth, *Earth and Planetary Science Letters*, **578**, 117329, https://doi.org/10.1016/j.epsl.2021.117329.

Murchie, S.L., Vervack, R.J. Jr, Ernst, C.M., Strom, R.G., Mercury. *In: Encyclopedia of the Solar System (Third Edition), Academic Press*, ISBN: 978-0-12-415845-0, p. 283-304

Ness, N.F., Acuña, M.H., Burlaga, L.F., Connerney, J.E.P., Lepping, R.P.; Neubauer, F.M., 1989, Magnetic Fields at Neptune. *Science*. **246** (4936): 1473–78. doi:10.1126/science.246.4936.

NOAA, 2025, World Magnetic Model (WMM), https://www.ncei.noaa.gov/products/world-magnetic-model

Olson, P., Amit H. 2006, Changes in earth's dipole. *Naturwissenschaften.* **93**: 519–542 doi: 10.1007/s00114-006-0138-6

Ott H.W. (2009) EM Compatibility Engineering. John Wiley & Sons Inc., Hoboken. http://dx.doi.org/10.1002/9780470508510

Parkinson, W. D., 1983, Introduction to Geomagnetism, Scottish Academic Press, Edinburgh, ISBN: 0707302927, p. 308–340.

Pearl, J., Conrath, B., 1991, The albedo, effective temperature, and energy balance of Neptune, as determined from Voyager data. *Journal of Geophysical Research: Space Physics*. **96**, 921–30. doi:doi:10.1029/91ja01087.

Purcell , E.M., Morin D., 2013, Electricity and Magnetism, 3rd Edition, Cambridge University Press, ISBN 978-1-107-01402-2.

Rodgers, A. & Wahr, J., 1993. Inference of core-mantle boundary topography from ISC PcP and PKP traveltimes, *Geophys. J. Int.*, **115**, 991–1011.

Roman, M.T., Fletcher, L.N., Orton, G.S., Vatant d'Ollone, J., Sinclair, J.A., Rowe-Gurney, N., Moses, J.I., & Irwin, P.J., 2020, Sub-Seasonal Variations in Neptune's Stratospheric Infrared Emission from VLT-VISIR, 2006-2018. The Planetary Science Journal, 3, 41 pp, https://doi.org/10.3847/PSJ/ac5aa4

Schelkunoff S. A., 1943, EM Waves. Van Nostrand, New York, 530 pp.

Smithsonian Institution, 2025, Has volcanic activity been increasing? https://volcano.si.edu/faq/index.cfm?question=historicalactivity

Smrekar, S.E., Stofan, E.R., Müller, N., 2014, Venus: Surface and Interior. *In: Encyclopedia of the Solar System (Third Edition), Academic Press* ISBN: 978-0-12-415845-0, p. 323-341

Smith, P., Needham, J., 1967, Magnetic Declination in Mediaeval China. *Nature* **214**, 1213–1214 https://doi.org/10.1038/2141213b0

Soldati, G., Boschi, L., Forte, A., 2012, Tomography of core–mantle boundary and lowermost mantle coupled by geodynamics. *Geophys. J. Int.*, **189**, 730–746, https://doi.org/10.1111/j.1365-246X.2012.05413.x

Stacey, F., & Davis, P., 2008, Physics of the Earth (4th ed.). Cambridge: Cambridge University Press. doi:10.1017/CBO9780511812910

Stamper, R., Lockwood, M., Wild, M., Clark, T., 1999, Solar causes of the long-term increase in geomagnetic activity. *Journal of Geophysical Research*, **104,** 28325-28342. doi: doi.org/10.1029/1999JA900311

Stanley, S., 2014, Magnetic Field Generation in Planets. *In: Encyclopedia of the Solar System (Third Edition), Academic Press*, 121-135, ISBN: 978-0-12-415845-0

Stanley S., Bloxham, J., 2004, Convective-region geometry as the cause of Uranus' and Neptune's unusual magnetic fields. *Nature*. **428**(6979):151-3. doi: 10.1038/nature02376. PMID: 15014493.

Steinberger B., 2000, Plumes in a convecting mantle: Models and observations for individual hotspots. *Journal of Geophysical Research*. **105**. 11127-11152. https://doi.org/10.1029/1999JB900398.

Tkalčić, H., Phạm T., 2018, Shear properties of Earth's inner core constrained by a detection of J waves in global correlation wavefield. *Science*, **362**, 329-332, doi: 10.1126/science.aau7649

Turner, J. , Winch, D., Ivers, D., Stening, R., 2007, Regular daily variations in satellite magnetic total intensity data. *Annales Geophysicae,* **25**, 2167-2174.

Verhoogen, J., 1980, Energetics of the Earth. National Acad. of Sciences Collection, doi: 10.17226/9579

Vogel, K., 2025, The cause of the 100,000-year geomagnetic and climate cycles. https://doi.org/10.22541/essoar.174344800.02936683/v2

Wang, X., Li, L., Roman, M., et al., 2025, Internal Heat and Energy Imbalance of Uranus., arXiv:2502.20722v1 , https://doi.org/10.48550/arXiv.2502.20722

Weissman P.R., 2014, The Solar System and Its Place in the Galaxy. *In: Encyclopedia of the Solar System (Third Edition), Academic Press* ISBN: 978-0-12-415845-0, p. 3-28

Wu, C., Usoskin, I., Krivova, N., Kovaltsov, G., Baroni, M., Bard, E., Solanki, S., 2018, Solar activity over nine millennia: A consistent multi-proxy reconstruction. Astronomy & Astrophysics, **615**, doi:10.1051/0004-6361/20173

Zerbo, J-L., and Richardson, J., 2015, The solar wind during current and past solar minima and maxima, *J. Geophys. Res. Space Physics*, **120**, 10,250–10,256, doi:10.1002/2015JA021407.

Zimmer, C., Khurana, K.K., Kivelson, M.G., 2000, Subsurface Oceans on Europa and Callisto: Constraints from Galileo Magnetometer Observations. *Icarus*, **147**, 329-347.